DOI: 10.26599/FSHW.2026.9250913

Contents lists available at SciOpen

Food Science and Human Wellness

journal homepage: https://www.sciopen.com/journal/2097-0765

China Food Publishing Co.

Tiliroside Alleviates Atherosclerosis by Promoting Cholesterol Efflux via SYK Inhibition: Integrated Multi-Omics, Machine Learning, Molecular Simulation, and In Vivo/In Vitro Validation

Runwen Li[1,2†], Huqiang He[1,5†], Xiaoyuan Guo [1], Daifang Zhang[1,3], Ruilin Zhang[1], Jiqiang Li[1], Hao Chen[1], Yong Liu[1,3,4,5*] and Ya Wu[1,3*]

[1] *Department of Vascular Surgery, The Affiliated Hospital, Southwest Medical University, Luzhou, 646000, China*

[2] *Department of Vascular Diseases, Panzhihua Central Hospital, Panzhihua, 617000, China*

[3] *Metabolic Vascular Disease Key Laboratory of Sichuan Province, The Affiliated Hospital, Southwest Medical University, Luzhou, 646000, China*

[4] *Key Laboratory of Medical Electrophysiology, Ministry of Education & Medical Electrophysiological Key Laboratory of Sichuan Province (Collaborative Innovation Center for Prevention of Cardiovascular Diseases), Institute of Cardiovascular Research, Southwest Medical University, Luzhou, 646000, China*

[5] *Department of General Surgery, The Affiliated Hospital, Southwest Medical University, Luzhou, 646000, China*

ABSTRACT: Background: Atherosclerosis (AS) is a chronic inflammatory vascular disease, and its progression is closely associated with immune dysregulation and lipid metabolic disorders. Natural active compounds, as multi-target therapeutic agents, have shown promising potential in the prevention and treatment of cardiovascular diseases. Tiliroside (Tle), a natural flavonoid with anti-inflammatory and antioxidant properties, exhibits potential therapeutic effects against AS; however, its molecular mechanisms remain poorly understood. **Methods:** In this study, we employed an integrated strategy combining animal models, transcriptomic data mining, target prediction, molecular docking, molecular dynamics simulations, single-cell transcriptomic analysis, and multiple machine learning algorithms to systematically identify and validate the key targets of Tle. Both in vivo and in vitro experiments were conducted to explore its underlying mechanisms in AS intervention. **Results:** Tle significantly attenuated atherosclerotic lesion development in ApoE$^{-/-}$ mice, reduced lipid accumulation and inflammatory cytokine expression, and exhibited favorable safety. Multi-omics integration identified spleen tyrosine kinase (SYK) as a potential core target. Molecular simulations revealed that Tle binds stably to SYK, effectively inhibiting its phosphorylation, promoting cholesterol efflux, and suppressing foam cell formation and inflammatory responses. Single-cell analysis further demonstrated that SYK is predominantly expressed in macrophages within AS tissues. Functional experiments confirmed that SYK plays a key mediating role in the atheroprotective effects of Tle. **Conclusion:** This study systematically elucidates the critical role of SYK in the pathogenesis of AS and, for the first time, proposes and validates the "Tle–SYK–Macrophage" regulatory axis. These findings reveal the dual regulatory role of Tle in modulating immune and metabolic pathways to alleviate AS, providing new insights and potential targets for natural product-based therapeutic strategies.

† Both Runwen Li and Huqiang He made equal contributions to this work.
***Co-corresponding author**
Ya Wu, E-mail: yawu@swmu.edu.cn
Yong Liu, E-mail: lyong74@swmu.edu.cn

Received 29 June 2025
Received in revised from 23 August 202
Accepted 10 September 2025

Keywords: Atherosclerosis; Tiliroside; SYK; Bioinformatics; Cholesterol Efflux

1. Introduction

Cardiovascular diseases (CVDs) have become one of the leading contributors to the global disease burden. According to the Global Burden of Disease (GBD) study, the worldwide prevalence of CVDs increased significantly from 271 million in 1990 to 523 million in 2019, with related deaths accounting for approximately one-third of total global mortality[1, 2]. Atherosclerosis (AS), the primary pathological basis of CVDs, involves multiple mechanisms during its initiation and progression, including lipid metabolism disorders, chronic inflammation, and vascular wall remodeling[3, 4]. Currently, first-line clinical treatments primarily rely on statins, which lower serum low-density lipoprotein cholesterol (LDL-C) levels by inhibiting 3-hydroxy-3-methylglutaryl-coenzyme A (HMG-CoA) reductase activity[5, 6]. However, long-term statin use may lead to adverse effects such as hepatotoxicity, myopathy, and gastrointestinal disturbances, thereby reducing patient adherence[7, 8]. As a result, the development of low-toxicity and highly effective natural therapeutic alternatives has emerged as a key research focus in the prevention and treatment of AS.

Tiliroside, a flavonoid glycoside commonly found in plants of the Tiliaceae and Rosaceae families, features a unique C-glycosidic bond structure that confers high in vivo stability and favorable bioavailability[9-11]. Previous studies have demonstrated that Tiliroside exerts significant protective effects in models of AS-related diseases, including metabolic syndrome and endothelial dysfunction. These effects are mediated through multiple mechanisms, such as inhibition of the nuclear factor-κB (NF-κB) inflammatory pathway, activation of AMP-activated protein kinase/mechanistic target of rapamycin (AMPK/mTOR) signaling, and scavenging of reactive oxygen species (ROS)[12-14]. Importantly, its metabolites exhibit minimal cytotoxicity and are primarily excreted via urine and feces, presenting a low risk of bioaccumulation and offering superior biosafety compared to conventional chemical drugs[15, 16]. Although previous research has highlighted its potential in regulating inflammation and lipid/glucose metabolism, the precise mechanisms by which Tiliroside modulates the onset and progression of atherosclerosis (AS) remain to be fully elucidated.

The formation of foam cells is a key pathological event in the initiation and progression of atherosclerosis (AS), primarily resulting from impaired cholesterol metabolism within macrophages[17, 18]. In the early stages of AS, endothelial barrier dysfunction permits low-density lipoprotein (LDL) to infiltrate the vascular intima, where it undergoes oxidative modification to form oxidized LDL (ox-LDL)[19]. Ox-LDL is internalized by macrophages via scavenger receptors such as CD36, SR-A, and LOX-1, subsequently accumulating within the cells and promoting foam cell formation[20-22]. Cholesterol within macrophages can be esterified into cholesterol esters for storage by acyl-CoA:cholesterol acyltransferase-1 (ACAT-1) or exported via membrane transporters, including ATP-binding cassette transporters A1 (ABCA1), G1 (ABCG1), and scavenger receptor class B type 1 (SR-B1), to maintain intracellular cholesterol homeostasis[19, 23, 24]. Spleen tyrosine kinase (SYK), a non-receptor tyrosine kinase, plays a central role in immune signal transduction and functions as a key downstream effector in several pattern recognition

receptor (PRR) pathways, including Toll-like receptors (TLRs), Fc gamma receptors (FcγRs), and Dectin-1, thereby contributing to inflammatory activation and immune regulation[25]. Recent studies have shown that inflammatory conditions suppress liver X receptor alpha (LXRα)-mediated cholesterol transport, leading to reduced expression of ABCA1 and ABCG1, impaired cholesterol efflux, and increased foam cell accumulation[26, 27]. Under such conditions, elevated SYK activity may further disrupt cholesterol efflux pathways by amplifying inflammatory signaling, highlighting its crucial regulatory role in cholesterol metabolic disorders associated with AS.

In elucidating the mechanisms of natural drug actions and identifying novel therapeutic targets, the integration of bioinformatics, machine learning, and molecular simulations has emerged as a critical strategy to address the complexity of multi-omics data and the heterogeneity of disease networks[28]. Bioinformatics techniques enable differential gene expression analysis, pathway enrichment, and network topology modeling based on transcriptomic and single-cell transcriptomic data, thereby identifying key pathways and candidate targets associated with disease progression (e.g., employing weighted gene co-expression network analysis [WGCNA] to detect disease-related modules)[29, 30]. Machine learning, through both supervised and unsupervised algorithms, facilitates the modeling of high-dimensional, nonlinear data, thereby improving the efficiency of feature gene selection and target prioritization[31]. Molecular docking and molecular dynamics simulations further validate the binding modes and structural stability between small molecules and protein targets, creating a feedback loop from virtual screening to mechanism prediction in structural biology research[32, 33]. On this basis, the present study investigates Tiliroside as a candidate natural therapeutic agent. By combining bioinformatics analysis, machine learning-based target screening, molecular docking, and molecular dynamics simulations with in vivo and in vitro functional experiments, we systematically explore the effects of Tiliroside on AS progression and elucidate its potential molecular mechanisms from multiple levels.

2. Materials and Methods

2.1 Reagents and Chemicals

Tiliroside (Tle, CAS No. 20316-62-5, HPLC purity ≥98%) was purchased from Chengdu Lemitian Pharmaceutical Technology Co., Ltd. (Chengdu, China). Oxidized low-density lipoprotein (Ox-LDL) (Catalog No. YB-002) was obtained from Guangzhou Yiyuan Biotechnology Co., Ltd. (Guangzhou, China) and was used to construct the foam cell model. Oil Red O staining kits (Catalog No. G1016), as well as mouse IL-6 (Catalog No. MM-0163M2), IL-1β (Catalog No. MM-0040M1), and TNF-α (Catalog No. MM-0132M1) ELISA kits, were purchased from Meimian Biotech Co., Ltd. (Nanjing, China) for detecting the expression levels of pro-inflammatory factors. Total cholesterol assay kits (Catalog No. BC1985) and free cholesterol assay kits (Catalog No. BC1895) were purchased from Beijing Solarbio Science & Technology Co., Ltd. (Beijing, China) to assess intracellular lipid metabolism changes. LipoRNAi™ transfection reagent (Catalog No. C0535) was purchased from Shanghai Biotime Biotechnology Co., Ltd. (Shanghai, China) for siRNA transfection experiments. For the Western blot experiments, primary

antibodies used included mouse anti-SYK monoclonal antibody (Catalog No. sc-390806, Santa Cruz Biotechnology, USA) and rabbit anti-p-SYK polyclonal antibody (Catalog No. ab58575, Abcam, UK). HRP-conjugated secondary antibodies included goat anti-mouse IgG-HRP (Catalog No. ZB-2305) and goat anti-rabbit IgG-HRP (Catalog No. ZB-2301), both purchased from Zhongshan Golden Bridge Biotechnology Co., Ltd. (Beijing, China).

2.2 Identification and Functional Annotation of Potential Targets of Tiliroside

The three-dimensional structure of Tiliroside (PubChem CID: 5320686) was obtained in SDF format from the PubChem database and subjected to energy minimization (1000 steps) using the MMFF94 force field implemented in Open Babel v3.1.1 to optimize its conformation. Potential target prediction was conducted using a multi-database strategy, integrating data from the Comparative Toxicogenomics Database (CTD, 2024 version), SuperPred, SwissTargetPrediction (confidence score ≥ 0.7), and ChEMBL (v35). The resulting targets were standardized using UniProt (release 2024_01), with duplicates removed and gene symbols unified via the dplyr package in R. Functional annotation of the curated targets was carried out using the clusterProfiler package (v4.4.0). Gene Ontology (GO) enrichment analysis was conducted across three categories: Biological Process (BP), Cellular Component (CC), and Molecular Function (MF). Kyoto Encyclopedia of Genes and Genomes (KEGG) pathway enrichment analysis was performed using hypergeometric testing, with false discovery rate (FDR) correction applied via the Benjamini–Hochberg method (FDR < 0.05). All enrichment results were visualized using Metware Cloud (v2.1), including GO bubble plots, KEGG bar plots, and target–pathway interaction networks, to ensure intuitive presentation and reproducibility.

2.3 Screening and Functional Analysis of Differentially Expressed Genes in Atherosclerotic Plaques

To investigate the molecular mechanisms underlying atherosclerosis (AS), the transcriptomic dataset GSE100927 (Accession: GSE100927) was retrieved from the NCBI Gene Expression Omnibus (GEO) database[34]. This dataset comprises 69 atherosclerotic plaque samples and 25 normal arterial control samples, all confirmed by pathological diagnosis and accompanied by complete clinical information, including age, sex, and cardiovascular risk factors. Data preprocessing was performed using the limma package (v3.48.3) in R, including background correction (RMA algorithm), quantile normalization, and probe-to-gene mapping, resulting in a standardized expression matrix covering 28,869 genes. Differentially expressed genes (DEGs) were identified using the empirical Bayes linear modeling framework of limma. Specifically, a linear model was constructed with group variables (AS vs. control) as fixed effects, followed by moderated t-tests to calculate $\log_2$ fold changes ($\log_2$FC) and p-values. Multiple testing correction was applied using the Benjamini–Hochberg method. DEGs were defined using the thresholds $|\log_2 FC| > 1$ and adjusted p-value < 0.01. To further characterize the functional implications of DEGs, Gene Set Enrichment Analysis (GSEA) was performed using GSEA software (v4.3.2), referencing the C5 Canonical Pathways gene sets from the Molecular Signatures Database (MSigDB)[35]. The gene expression matrix and group

labels were used as input to evaluate enrichment trends of DEGs across various signaling pathways, thereby providing insight into aberrant biological processes in AS tissues from a functional perspective.

2.4 Construction and Module Identification of Atherosclerosis-Related Gene Co-expression Network Using WGCNA

To elucidate the coordinated regulatory patterns of gene expression during atherosclerosis (AS), the GSE100927 dataset was analyzed using Weighted Gene Co-expression Network Analysis (WGCNA) to construct a gene co-expression network and identify key modules[36]. Quality control was first performed on the gene expression matrix, and a sample clustering dendrogram was generated using the *sampleTree* function. Sample similarity was evaluated based on Euclidean distance, and a height cutoff threshold was applied to identify and remove outlier samples. Pairwise Pearson correlation coefficients were then calculated with the *cor* function to generate a correlation matrix, which was subsequently transformed into a topological overlap matrix (TOM) using the *TOM similarity* function to improve network robustness. To determine the soft-thresholding power (β), the *pickSoftThreshold* function was used to assess the scale-free topology fit index and mean connectivity across a range of candidate β values. Considering both scale-free topology and biological relevance, $\beta = 9$ was selected, achieving a scale-free topology fit index of $R^2 > 0.9$ while maintaining mean connectivity within a biologically reasonable range. This indicated that the constructed network exhibited a strong scale-free property and followed a power-law distribution with a slope of $\gamma = -1.82$. Network construction and module detection were performed using the *blockwiseModules* function with parameters set to deepSplit = 2 and minModuleSize = 30. Genes were partitioned into distinct co-expression modules using the dynamic tree cut algorithm, with each module assigned a unique color label. The module eigengene (ME)—defined as the first principal component of each module—was then calculated to represent the overall expression profile of each module, serving as the basis for downstream correlation analyses.

2.5 Molecular Docking and Molecular Dynamics Simulation of Tiliroside Interactions with Target Proteins

In the molecular docking stage, AutoDock v4.2.6 was used to preprocess both protein and ligand structures[37]. The protein structure was prepared by removing crystallographic water molecules, adding polar hydrogen atoms, and assigning Gasteiger charges, and subsequently converted into PDBQT format. The three-dimensional structure of the small-molecule ligand Tiliroside (PubChem CID: 5320686) was obtained from the PubChem database, converted using Open Babel, and incorporated into the docking workflow. The selected hub protein (e.g., SYK) served as the docking target, and a grid box was defined around its known active site. AutoDock Vina was then used to predict binding conformations and calculate binding affinities of Tiliroside with the protein target[38]. Based on the optimal docking conformation, a 100 ns molecular dynamics (MD) simulation of the Tiliroside–SYK complex was conducted using GROMACS 2022. Missing residues in the protein structure were repaired and energy minimized using Swiss-PdbViewer. The ligand was processed with PyMOL, saved in MOL2 format, and parameterized with Sobtop to generate GROMACS-compatible topology files. The simulation system was built with the CHARMM36 force field

for protein parameterization and solvated using the SPC/E water model. CHARMM36 was chosen for its proven accuracy and broad applicability in maintaining protein conformational stability and reproducing protein–ligand interaction dynamics. Ligand parameters were generated using the CHARMM General Force Field (CGenFF), ensuring compatibility with the protein force field. The system was further refined by adding 0.15 mol/L NaCl to maintain electrostatic neutrality, followed by energy minimization (steepest descent) and equilibration under NVT (constant volume and temperature) and NPT (constant pressure and temperature) ensembles. Finally, a 100 ns production MD simulation was performed to evaluate the dynamic stability and interaction patterns of the complex in an aqueous environment. The simulation trajectory analysis involved the following metrics:

Root Mean Square Deviation (RMSD): to assess the overall structural stability of the complex.

Radius of Gyration (Rg): to evaluate the compactness of the protein structure.

Root Mean Square Fluctuation (RMSF): to analyze the flexibility of the residues.

Hydrogen Bond Analysis: to track the frequency of hydrogen bond formation between the protein and ligand throughout the simulation[39].

2.6 Identification of Potential Core Target Genes Using Machine Learning Algorithms

To further identify core target genes potentially involved in the therapeutic effects of Tiliroside in atherosclerosis, three mainstream machine learning algorithms were employed: Least Absolute Shrinkage and Selection Operator (LASSO), Support Vector Machine–Recursive Feature Elimination (SVM-RFE), and Random Forest. Integrating multiple algorithms aimed to enhance the accuracy and robustness of feature selection. LASSO Regression Analysis: LASSO regression was performed using the glmnet package (v4.1.2) in R to perform variable compression and selection. The optimal regularization parameter (λ) was determined via 10-fold cross-validation, enabling the identification of a representative gene feature set[40]. SVM-RFE Analysis: The SVM-RFE algorithm was implemented using the e1071 and caret packages in R, with the svmRadial function. This method evaluated model performance by sequentially eliminating less informative variables, ultimately identifying the most discriminative gene features. Random Forest Analysis: The Random Forest algorithm was used to rank gene features by importance. Through the construction of multiple decision trees and ensemble learning, the contribution of each gene to the model's predictive performance was quantified, thereby identifying critical variables for classification[41]. To comprehensively evaluate the classification performance of the three algorithms in core gene identification, receiver operating characteristic (ROC) curves were generated and the area under the curve (AUC) was calculated[42]. This enabled comparison of the predictive accuracy and generalization capabilities across models. Finally, genes that consistently demonstrated high performance across all three algorithms were selected as key candidate targets for subsequent functional annotation and experimental validation.

2.7 Multi-Algorithm Integrated Analysis of the Association Between Atherosclerosis Immune Microenvironment and Core Target Genes

To systematically explore the potential associations between core target genes and the immune microenvironment in atherosclerosis (AS), a combination of CIBERSORT, ESTIMATE, and Spearman's rank correlation analysis was employed to characterize immune infiltration patterns[43, 44]. Using transcriptomic data from 69 AS plaque samples and 23 control arterial tissue samples in the GSE100927 dataset, the relative proportions of 22 immune cell subsets were estimated for each sample using the CIBERSORT algorithm (v1.03, https://cibersortx.stanford.edu/). The analysis was based on the LM22 signature gene matrix, with 1000 Monte Carlo permutations conducted to improve estimation robustness. Only samples with a confidence P-value < 0.05 were retained for downstream analysis. In parallel, the ESTIMATE algorithm (v1.0.9) was applied to evaluate the overall levels of immune and stromal cell infiltration in AS tissues. This yielded three scoring indices—Immune Score, Stromal Score, and ESTIMATE Score—to quantify non-tumor microenvironment components such as immune cells and fibroblasts. For the core target genes SYK and CCR1, identified through machine learning, Spearman's rank correlation analysis was used to assess their association with immune cell abundance. Correlation significance was defined by a threshold of $|\rho| > 0.3$ and $P < 0.05$. A heatmap was generated to visualize the correlation network between core genes and immune cell subsets, thereby elucidating their potential regulatory roles within the immune microenvironment.

2.8 Single-Cell Transcriptomic Data Analysis

To investigate the cell-type-specific expression profile of SYK in atherosclerotic (AS) tissue, single-cell transcriptomic data from the publicly available GSE159677 dataset were obtained from the GEO database. Raw sequencing data were processed using the Seurat package (v4.3.0) in R, including quality control, normalization, selection of highly variable genes, and batch effect correction[45]. Low-quality cells were filtered out based on predefined thresholds, such as a mitochondrial gene proportion >10% and fewer than 200 detected genes. Principal component analysis (PCA) was performed on the highly variable genes, and a nearest-neighbor graph was constructed using the top 20 principal components. Cell clustering was carried out using the Louvain algorithm. The Uniform Manifold Approximation and Projection (UMAP) method was applied for dimensionality reduction and visualization, resulting in the identification of eight major cell subpopulations. Cell-type annotation was based on the expression of canonical marker genes: monocytes (LYZ, FCN1), macrophages (C1QA, C1QB, C1QC), T cells (CCL5, IL7R), B cells (MS4A1), smooth muscle cells (ACTA2, TAGLN, MYL9), fibroblasts (COL1A1), endothelial cells (PECAM1, VWF), and mast cells (TPSB2). Based on this annotation, SYK expression patterns were assessed across different cell clusters to determine its distribution within AS tissues. To compare differences between AS and control samples, metadata grouping information was extracted. Proportions of each cell type and SYK expression levels were statistically analyzed between groups. UMAP feature plots and boxplots were generated to evaluate the cell-type specificity and differential expression of SYK, particularly in macrophages. Additionally, heatmaps of the top five marker genes per cluster were generated using the DoHeatmap function to validate the accuracy of cell-type annotation.

Total RNA was extracted using the Total RNA Purification Kit (Catalog No. 5003050; Hangzhou Xinjing Biotechnology Development Co., Ltd., China), following the manufacturer's protocol. Complementary DNA (cDNA) was synthesized using the ExonScript RT SuperMix with dsDNase Kit (Catalog No. A502-01; Chengdu Rongwei Gene Biotechnology Co., Ltd., China), ensuring efficient reverse transcription and elimination of genomic DNA contamination. Quantitative real-time PCR (qRT-PCR) was performed using the Fast SYBR Green qPCR Master Mix UDG Kit (Catalog No. A402-01; Chengdu Rongwei Gene Biotechnology Co., Ltd., China), with reaction preparation and thermal cycling conducted according to the manufacturer's instructions. β-actin was used as the internal reference gene to normalize target gene expression and account for variability in RNA input between samples. Relative gene expression levels were calculated using the 2^−ΔΔCt method. Primer sequences are listed in Supplementary Table 1.

2.10 Oil Red O Staining for Detection of Lipid Deposition in Cells and Tissues

2.10.1 Lipid Staining in Macrophages

The mouse monocyte–macrophage cell line RAW264.7 was provided by the School of Pharmacy, Southwest Medical University. Cells were seeded at a density of 1×10^5 cells/well in 6-well plates and treated with 60 μg/mL oxidized low-density lipoprotein (ox-LDL) and varying concentrations of Tiliroside (10, 20, and 40 μmol/L) for 24 hours. After treatment, the medium was removed, and the cells were gently washed twice with PBS. Cells were then fixed with 4% paraformaldehyde for 10 minutes at room temperature. After fixation, 1 mL of 60% Oil Red O working solution (prepared by dissolving 0.5 g Oil Red O in 100 mL of 60% isopropanol and filtering through a 0.22 μm membrane) was added, and staining was performed in the dark for 20 minutes. Cells were washed twice with 60% isopropanol (1 minute each) to remove nonspecific staining, followed by three PBS washes. Stained cells were visualized under an inverted microscope (Olympus IX73) at 400× magnification. Lipid droplet accumulation was quantified using ImageJ software based on integrated optical density (IOD).

2.10.2 Lipid Staining in Mouse Aortic Tissue

Aortic tissue from ApoE$^{-/-}$ mice was embedded in OCT compound and cryosectioned into 5 μm-thick consecutive slices using a Leica CM1950 cryostat. Sections were mounted on glass slides, air-dried at room temperature for 30 minutes, and fixed in pre-cooled acetone (–20℃) for 10 minutes. After fixation, slides were stained with Oil Red O working solution in the dark for 20 minutes. Differentiation was performed using 60% isopropanol for 10 seconds, followed by three rinses with distilled water. Sections were counterstained with hematoxylin for 5 minutes, differentiated with 1% hydrochloric ethanol for 10 seconds, and blued under running tap water for 5 minutes. After dehydration and clearing, sections were mounted with neutral balsam and observed under a brightfield microscope (Nikon Eclipse 80i) at 200× magnification. Plaque area at the aortic root was quantified using Image-Pro Plus 6.0 software. The percentage of Oil Red O-positive area relative to the total lumen area was calculated. To ensure data reliability, three consecutive sections per mouse were analyzed, and the mean value was used for statistical evaluation.

2.11 Measurement of Cholesterol Efflux Rate

RAW264.7 macrophages were seeded in 24-well plates following either differentiation or siRNA transfection. The [^{3}H]-cholesterol working solution (final concentration: 0.5 μCi/mL) was prepared in RPMI-1640 medium supplemented with 0.5% fetal bovine serum (FBS) and added to each well. Cells were incubated at 37℃ for 48 hours to isotopically label the intracellular cholesterol pool. After incubation, cells were gently washed twice with PBS to remove unbound [^{3}H]-cholesterol. The medium was then replaced with serum-free RPMI-1640 containing either 25 μg/mL apolipoprotein A-I (apoA-I) or 50 μg/mL high-density lipoprotein (HDL). Cells were incubated overnight at 37℃ to induce cholesterol efflux. Following incubation, both culture supernatants and cell lysates were collected, and the radioactivity in each was measured using a liquid scintillation counter, expressed as counts per minute (CPM). The cholesterol efflux rate was calculated using the following formula:

Cholesterol efflux rate (%) = [CPM in the medium / (CPM in the medium + CPM in the cells)] × 100%

2.12 Cell Transfection

Two small interfering RNA (siRNA) sequences targeting distinct regions of the SYK gene mRNA (designated RNAi1 and RNAi2) were designed. The specific sequences are provided in Supplementary Table 2. An irrelevant siRNA targeting enhanced green fluorescent protein (EGFP), referred to as RNAi-EGFP, was used as a negative control (NC). All siRNAs were synthesized by Chengdu Aochuang Biotechnology Co., Ltd. RAW264.7 cells were seeded into 6-well plates at a density of 2 × 10^4 cells/well. Prior to transfection, 2 mL of complete growth medium containing serum and antibiotics was added to each well. For each transfection, 125 μL of serum- and antibiotic-free medium, 100 pmol of siRNA, and 4 μL of LipoRNAi transfection reagent were gently mixed in sterile microcentrifuge tubes (without vortexing or centrifugation) and incubated at room temperature to allow the formation of transfection complexes (stable for up to 6 hours).The complexes were added to the corresponding wells, gently mixed, and incubated at 37℃ with 5% CO_2. The experiment included three groups: blank control (Control), negative control (NC, RNAi-EGFP), and SYK interference groups (RNAi1 and RNAi2). Cells were cultured for 48 hours before being harvested for downstream analyses.

2.13 Western Blot Analysis of Protein Expression

Aortic tissue and RAW264.7 cells were lysed using RIPA lysis buffer supplemented with protease inhibitors. Tissues were homogenized, and cells were scraped and centrifuged at 12,000 × g for 15 minutes at 4℃. The supernatant was collected, and protein concentrations were measured using the BCA protein assay. Samples were mixed with 5× SDS loading buffer and denatured at 100℃ for 10 minutes. Equal amounts of protein (20 μL per lane) were separated by 10% SDS-PAGE and transferred to 0.22 μm polyvinylidene fluoride (PVDF) membranes (Millipore). Membranes were blocked with 5% non-fat milk in TBST for 1 hour at room temperature, then incubated overnight at 4℃ with the appropriate primary antibodies. After washing, membranes were incubated with HRP-conjugated secondary antibodies for 1 hour at room temperature. Protein bands were visualized using enhanced chemiluminescence (ECL) substrate

(Nanjing Nuovision), and images were captured using the ChemiDoc XRS+ imaging system. Band intensity was quantified using ImageJ software. β-actin was used as a loading control, and target protein expression levels were normalized to the corresponding β-actin intensity.

2.14 Immunofluorescence Staining

Paraffin-embedded tissue samples were sectioned to a thickness of 4–6 μm using a microtome and mounted onto glass slides. The sections were deparaffinized and rehydrated through the following steps: two washes in xylene (5–10 minutes each), followed by two washes in 100% ethanol (5 minutes each), and one wash in 95% ethanol (5 minutes). Slides were then rinsed with distilled water to remove residual ethanol. Antigen retrieval was performed using sodium citrate buffer, with heating under high-pressure steam for 20 minutes. After cooling to room temperature, the sections were washed three times with PBS (5 minutes each) to remove residual retrieval buffer. To block non-specific binding, sections were incubated with 5% normal goat serum at room temperature for 30 minutes. Appropriately diluted primary antibodies were then applied and incubated overnight at 4℃. The next day, slides were washed three times with PBS to remove unbound primary antibodies and then incubated with fluorescently labeled secondary antibodies for 1 hour at room temperature in the dark. Afterward, slides were washed again with PBS to remove excess secondary antibodies. Cell nuclei were counterstained with DAPI solution for 5–10 minutes, followed by a final PBS rinse. Sections were then mounted using anti-fade mounting medium and sealed with coverslips. Fluorescence images were acquired using a fluorescence microscope equipped with appropriate excitation and emission filters.

2.15 Experimental Animal Model Construction and Intervention Design

Eight-week-old male ApoE$^{-/-}$ mice (C57BL/6J background, body weight 20 ± 2 g) were used to establish an atherosclerosis model. Age-matched wild-type C57BL/6J mice served as the normal control group. All animals were obtained from the Animal Experimental Center of Southwest Medical University and housed in a specific pathogen-free (SPF) barrier facility under controlled environmental conditions (temperature: 25 ± 1℃; humidity: 40%–60%; 12-hour light/dark cycle), with free access to food and water. Prior to the experiment, mice were acclimatized for 7 days, during which body weight and general health were monitored daily. A total of 72 mice were stratified by body weight and randomly assigned to six groups (n = 12 per group) as follows:

Control group: Wild-type mice fed an atherogenic diet (containing 0.5% sodium cholate; Rodent Diet, Catalog No. SL0008);

Model group: ApoE$^{-/-}$ mice fed the same atherogenic diet;

Tiliroside low-dose group (L-Tle): ApoE$^{-/-}$ mice fed the atherogenic diet and administered tiliroside at 25 mg/kg;

Tiliroside medium-dose group (M-Tle): ApoE$^{-/-}$ mice fed the atherogenic diet and administered tiliroside at 50 mg/kg;

Tiliroside high-dose group (H-Tle): ApoE$^{-/-}$ mice fed the atherogenic diet and administered tiliroside at 100 mg/kg;

Positive control group (Ator): ApoE$^{-/-}$ mice fed the atherogenic diet and administered atorvastatin at 3 mg/kg.

Tiliroside, a naturally occurring flavonoid with anti-inflammatory, antioxidant, and lipid-modulating properties, was selected for pharmacological evaluation. Based on previous studies, tiliroside has demonstrated favorable bioactivity and safety in the dose range of 12.5–100 mg/kg in rodent models[46-49]. Therefore, three doses were chosen to investigate its dose-dependent effects:

25 mg/kg (low dose): to assess baseline activity;

50 mg/kg (medium dose): representing a commonly reported effective dose;

100 mg/kg (high dose): to evaluate potential dose-enhancement effects and safety margins.

Tiliroside was dissolved in DMSO and diluted with normal saline to achieve a final DMSO concentration of <1%. All treatments were administered via intraperitoneal injection twice per week. Mice in the control and model groups received equivalent volumes of normal saline. Atorvastatin (3 mg/kg) was selected as a positive control drug. As a classical HMG-CoA reductase inhibitor, atorvastatin is widely utilized in both basic and clinical studies of atherosclerosis[50]. Previous reports have demonstrated that this dose effectively lowers lipid levels and attenuates atherosclerotic lesion development in ApoE$^{-/-}$ mice, with high safety and reproducibility[51, 52]. Thus, it served to validate the experimental model and provide a benchmark for comparison with tiliroside treatment. After 16 weeks of intervention, mice were anesthetized by intraperitoneal injection of 1% sodium pentobarbital (50 mg/kg). Blood samples were collected from the retro-orbital sinus using heparin sodium as an anticoagulant. Serum was separated by centrifugation at 3000 × g for 15 minutes and stored at –80℃ for subsequent lipid profiling and inflammatory cytokine analysis. Following euthanasia, the thoracic aorta and aortic arch were excised, rinsed with PBS, and divided into two portions: one was fixed in 4% paraformaldehyde for histological examination, and the other was snap-frozen in liquid nitrogen and stored at –80℃ for molecular assays. All procedures involving animals were conducted in strict accordance with the Regulations for the Administration of Laboratory Animals and relevant institutional ethical guidelines. The study protocol was approved by the Animal Ethics Committee of Southwest Medical University (Approval No.: 010139-06).

3. Results and Analysis

3.1 Tiliroside Intervention Attenuates Atherosclerotic Lesion Progression in ApoE$^{-/-}$ Mice

To evaluate the therapeutic potential of Tiliroside in AS, ApoE$^{-/-}$ mice were subjected to a 16-week intervention. Body weight monitoring showed no significant differences among the model, Tiliroside-treated (25, 50, and 100 mg/kg), and positive control (atorvastatin, 3 mg/kg) groups (Figure S1A), suggesting no adverse impact on body weight at the administered doses. Gross anatomical inspection revealed intact aortic walls without visible plaques in the control group, while extensive white lipid plaques were observed in the model group. Tiliroside treatment at all doses, as well as atorvastatin, significantly reduced plaque burden,

with the most pronounced reduction observed in the high-dose Tiliroside group (Figure 1A). H&E staining further confirmed that Tiliroside and atorvastatin effectively mitigated arterial wall thickening and plaque formation seen in the model group (Figures 1B, D). Consistently, Oil Red O staining revealed marked lipid deposition in the model group, which was significantly reduced in both Tiliroside- and atorvastatin-treated groups. Notably, high-dose Tiliroside (H-Tle) demonstrated comparable, and in some metrics superior, efficacy to atorvastatin in attenuating plaque and lipid accumulation (Figures 1C, E). Histological analysis of major organs (heart, liver, spleen, lungs, kidneys) revealed no structural abnormalities or signs of toxicity, supporting the favorable systemic safety profile of Tiliroside across the tested dose range (Figure S1B). Serum lipid analysis showed that high-fat diet feeding significantly elevated TC, TG, and LDL-C levels, while Tiliroside, particularly at high dose, and atorvastatin significantly reduced these parameters (Figures 1F–H). Of note, high-dose Tiliroside achieved greater LDL-C reduction than atorvastatin. Pro-inflammatory cytokines IL-6, TNF-α, and IL-1β were also markedly elevated in the model group. Tiliroside treatment resulted in dose-dependent suppression of all three cytokines. High-dose Tiliroside exhibited anti-inflammatory effects that were comparable to atorvastatin and showed superior suppression of IL-6 and IL-1β levels (Figures 1I–K). Collectively, these results demonstrate that Tiliroside significantly attenuates atherosclerotic progression in ApoE$^{-/-}$ mice through dual regulation of lipid metabolism and inflammation, with the high-dose regimen achieving therapeutic efficacy comparable to, and in some aspects exceeding, that of atorvastatin, while maintaining excellent systemic safety.

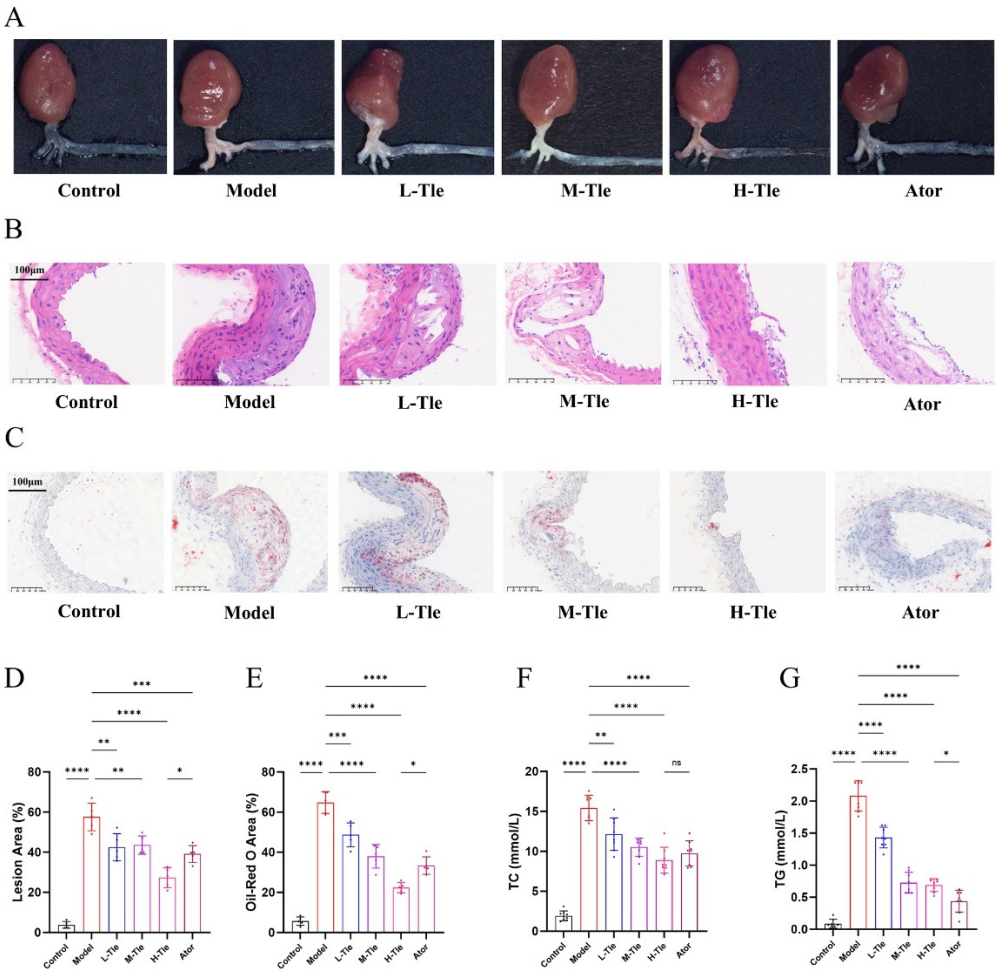

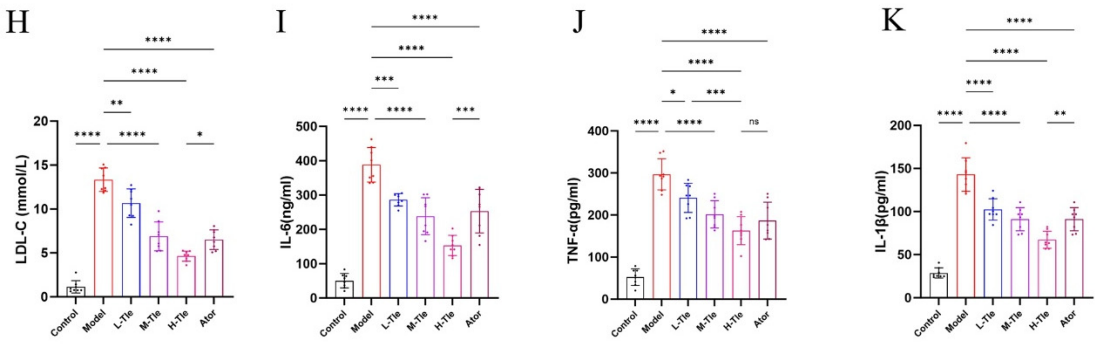

Figure 1. Tiliroside Attenuates Atherosclerotic Progression in ApoE$^{-/-}$ Mice

(A) Representative gross images of the aorta from different groups, showing varying degrees of plaque formation. (B) Hematoxylin and eosin (HE) staining of aortic tissue. The model group displayed pronounced intimal thickening and structural disorganization, whereas Tiliroside treatment markedly reduced neointimal hyperplasia and restored vascular integrity. High-dose Tiliroside (H-Tle) achieved superior efficacy compared with atorvastatin (Ator). (C) Oil Red O staining revealed extensive lipid deposition in the model group, which was reduced in a dose-dependent manner by Tiliroside, with greater improvement in the H-Tle group than in the Ator group. (D–E) Quantification of lesion area and Oil Red O–positive area confirmed significant reductions in both Tiliroside- and Ator-treated mice compared with the model group. (F–H) Serum lipid profiles showed that Tiliroside significantly lowered total cholesterol (TC), triglycerides (TG), and low-density lipoprotein cholesterol (LDL-C), with effects comparable to Ator. (I–K) ELISA results demonstrated that Tiliroside markedly suppressed IL-6, TNF-α, and IL-1β expression, indicating strong anti-inflammatory activity. Notably, the H-Tle group exhibited stronger effects than Ator. Data are presented as mean ± standard deviation (Mean ± SD). Statistical significance: $^{*}P < 0.05$, $^{**}P < 0.01$, $^{**}{}^{*}P < 0.001$, $^{****}P < 0.0001$.

3.2 Prediction of Potential Targets of Tiliroside and Functional Enrichment Analysis

To systematically elucidate the potential mechanisms of Tiliroside, target prediction was performed by integrating multiple databases. SwissTargetPrediction (confidence threshold ≥ 0.7) identified 105 candidate targets, while ChEMBL (v35) yielded 13 targets based on bioactivity data. Additionally, SuperPred and the Comparative Toxicogenomics Database (CTD) each predicted 2 targets. After data consolidation and standardization using the UniProt database (version 2024_01) and removal of duplicates, a final set of 116 unique human protein-coding genes was identified as potential targets of Tiliroside (Figure 2A). Subsequently, Kyoto Encyclopedia of Genes and Genomes (KEGG) pathway enrichment analysis was conducted on the predicted targets. Using hypergeometric testing with Benjamini–Hochberg correction (FDR < 0.05), several significantly enriched pathways were identified, including the chemokine signaling pathway, AGE–RAGE signaling pathway in diabetic complications, and HIF-1 signaling pathway (Figure 2B). These pathways are critically involved in immune cell migration, vascular inflammation, and hypoxic responses—key pathological processes in atherosclerosis. This suggests that Tiliroside may exert anti-atherosclerotic effects by modulating immune-inflammatory responses and oxygen homeostasis. In addition, Gene Ontology (GO) enrichment analysis was performed from three perspectives: Biological Process (BP), Cellular Component (CC), and Molecular Function (MF). BP enrichment revealed that the targets were primarily involved in cell signaling, metabolic regulation, and inflammation-related processes. CC analysis indicated that the targets were predominantly localized in the cytoplasm and nucleus, while MF enrichment was mainly associated with enzyme activity regulation and receptor–ligand binding (Figure 2C).

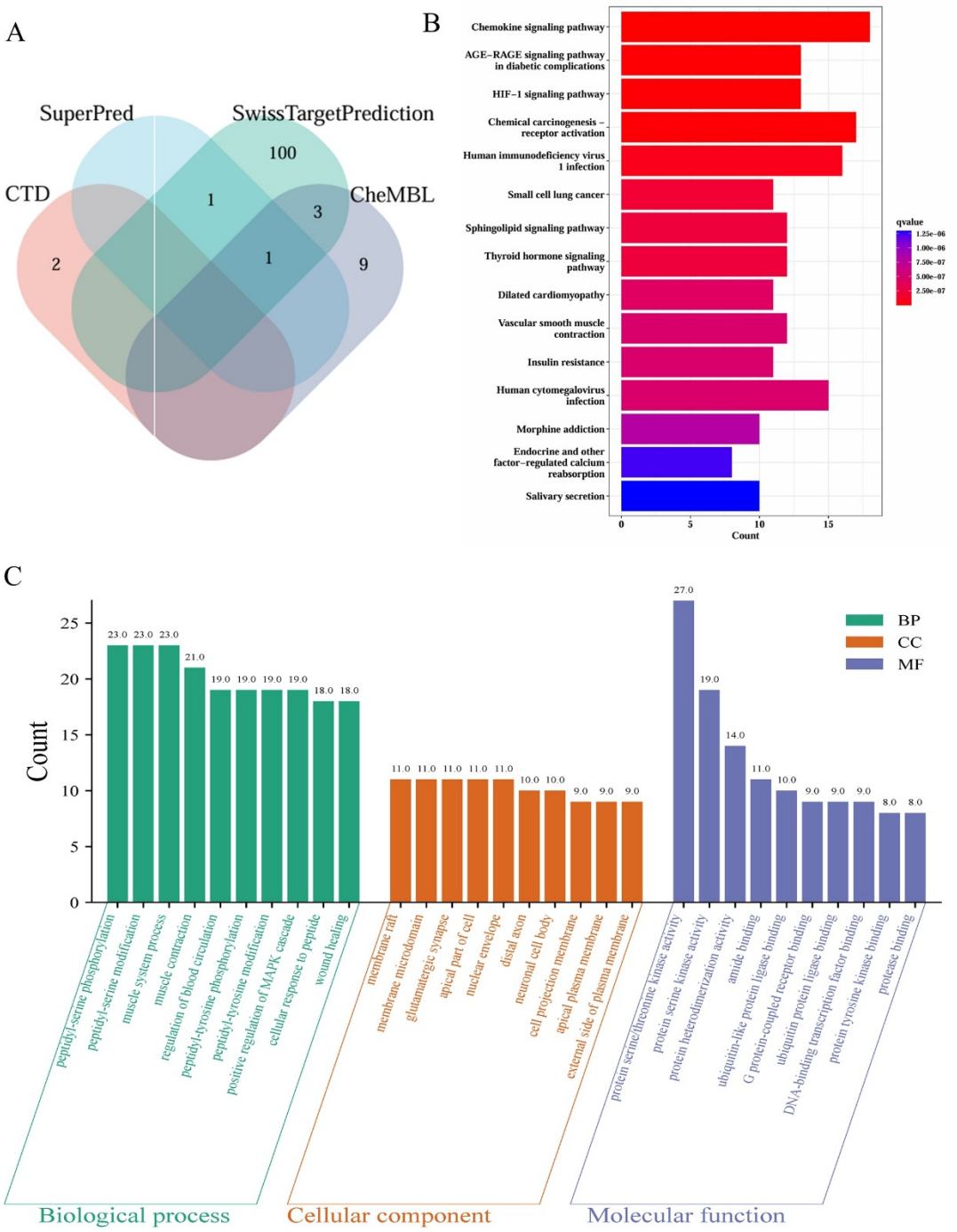

Figure 2. Prediction and Functional Enrichment of Tiliroside's Potential Targets

(A) Venn diagram summarizing predicted targets obtained from four databases: SwissTargetPrediction, ChEMBL (v35), SuperPred, and the Comparative Toxicogenomics Database (CTD). A total of 116 non-redundant protein-coding genes were identified after de-duplication and standardization. (B) KEGG pathway enrichment analysis of the predicted targets. The bar chart shows significantly enriched pathways, with the number of involved targets on the x-axis. Color intensity corresponds to statistical significance (q-value), with deeper red indicating higher significance. (C) Gene Ontology (GO) functional annotation of Tiliroside targets across three categories: Biological Process (BP, green), Cellular Component (CC, orange), and Molecular Function (MF, blue). The x-axis represents the number of genes enriched in each category.

3.3 Differential Gene Expression Analysis Reveals Prominent Immune Activation in Atherosclerotic Tissues

To comprehensively characterize the molecular features of atherosclerotic (AS) tissues, differential gene expression analysis was performed using the GSE100927 transcriptomic dataset, comparing AS tissues with normal control (Con) samples. The heatmap (Figure 3A) revealed that numerous representative genes were significantly upregulated in the AS group (red) and relatively downregulated in the control group

(blue), indicating widespread transcriptional activation in AS tissues. The volcano plot further illustrated the global distribution of differentially expressed genes (DEGs) (Figure 3B). To explore the biological significance of the DEGs, Gene Set Enrichment Analysis (GSEA) was conducted. The results showed significant enrichment of immune-related pathways in AS tissues, including antigen processing and presentation (KEGG_ANTIGEN_PROCESSING_AND_PRESENTATION), graft-versus-host disease (KEGG_GRAFT_VERSUS_HOST_DISEASE), and natural killer cell-mediated cytotoxicity (KEGG_NATURAL_KILLER_CELL_MEDIATED_CYTOXICITY) (Figure 3C). These enriched pathways suggest heightened immune cell infiltration and activation, enhanced antigen presentation, increased lysosomal activity, and cytotoxic responses—hallmarks of inflammatory processes. In contrast, normal control tissues were enriched in pathways related to cardiovascular function and metabolic homeostasis, such as dilated cardiomyopathy (KEGG_DILATED_CARDIOMYOPATHY) and cytochrome P450-mediated drug metabolism (KEGG_DRUG_METABOLISM_CYTOCHROME_P450) (Figure 3D), reflecting a physiological state of vascular and metabolic equilibrium. In summary, transcriptomic analysis of the GSE100927 dataset indicates that AS tissues exhibit pronounced immune-inflammatory activation, whereas normal tissues maintain a homeostatic profile centered on vascular and metabolic regulation. These findings support the hypothesis that immune dysregulation plays a pivotal role in the pathogenesis of atherosclerosis.

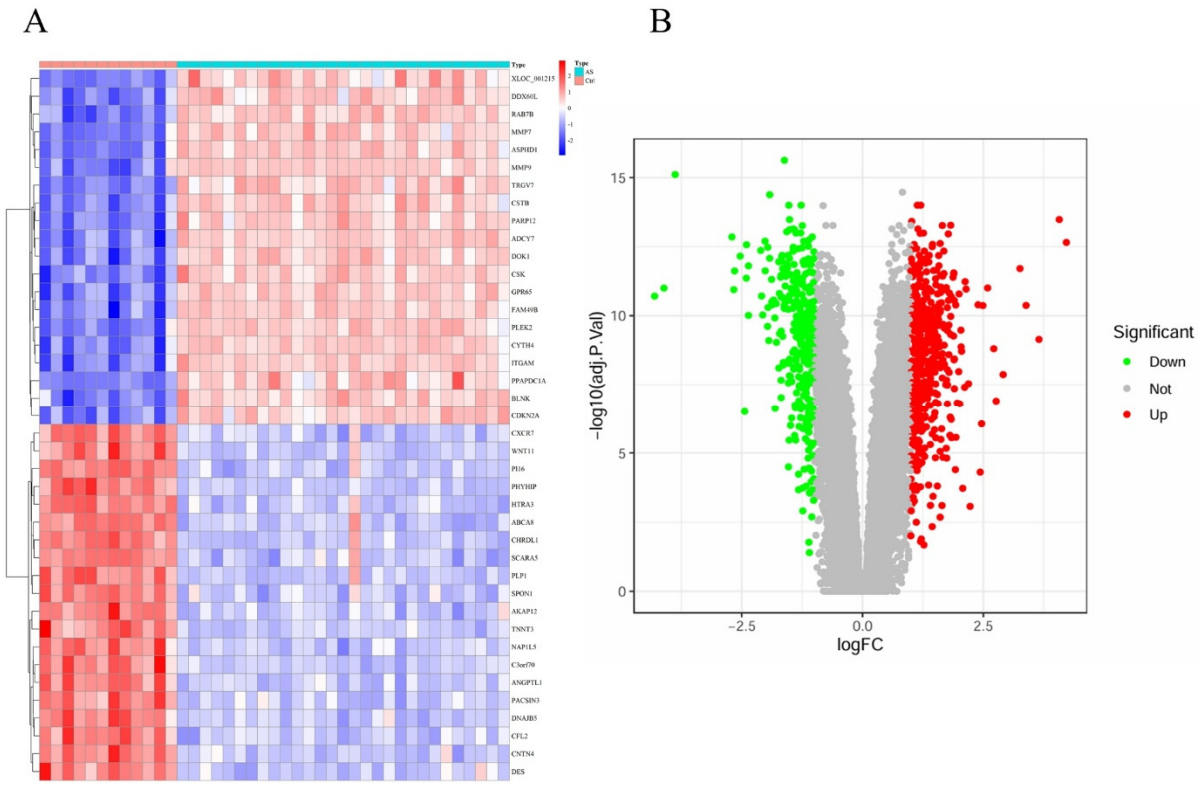

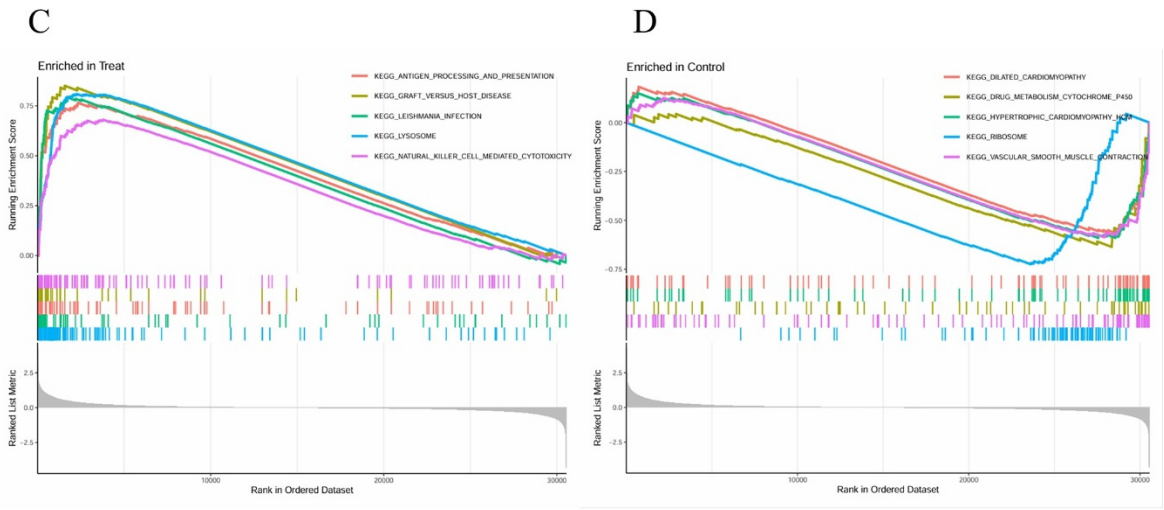

Figure 3. Differential Gene Expression and GSEA Analysis between Atherosclerotic and Normal Tissues
(A) Heatmap of representative differentially expressed genes (DEGs) between atherosclerotic (AS) and control (Ctrl) tissues. Red indicates upregulated genes; blue indicates downregulated genes. (B) Volcano plot of DEGs. Red and green dots represent significantly upregulated and downregulated genes, respectively, while gray dots denote non-significant genes. (C) Gene Set Enrichment Analysis (GSEA) identifies immune-related pathways significantly enriched in AS tissues, including Antigen Processing and Presentation, Graft-versus-Host Disease (GVHD), and Natural Killer (NK) Cell-Mediated Cytotoxicity. (D) GSEA of control tissues reveals enrichment in vascular and metabolic homeostasis pathways, such as Dilated Cardiomyopathy (DCM) and Cytochrome P450–Mediated Metabolism.

3.4 WGCNA Identifies the MEturquoise Module as a Key Co-expression Network Associated with Atherosclerosis

To further investigate gene modules functionally associated with atherosclerosis (AS), Weighted Gene Co-expression Network Analysis (WGCNA) was applied to the GSE100927 dataset. The top 6,000 genes with the highest variance in expression were selected to enhance the biological relevance and representativeness of the constructed network. Sample clustering analysis confirmed the absence of significant outliers, ensuring the quality of the input data for network construction (Figure 4A). Using soft-thresholding analysis, a β value of 9 was identified as optimal. The resulting network conformed to a scale-free topology ($R^2 > 0.9$, slope $\gamma = -1.82$) and maintained strong connectivity (Figures 4B, C). Genes were subsequently grouped into modules using the dynamic tree-cutting algorithm, with each module assigned a distinct color (Figure 4D). Module–phenotype correlation analysis identified the turquoise module (MEturquoise) as the most significantly associated with the AS phenotype, showing a strong positive correlation with AS ($r = 0.92$, $p = 8 \times 10^{-16}$) and a strong negative correlation with control samples ($r = -0.92$, $p = 8 \times 10^{-16}$) (Figure 4E). Further analysis revealed a high correlation between Module Membership (MM) and Gene Significance (GS) within the MEturquoise module ($r = 0.96$, $p < 1 \times 10^{-200}$), indicating that genes in this module are not only structurally co-expressed but also functionally relevant to AS (Figure 4F). These findings suggest that the MEturquoise module contains critical regulatory genes potentially involved in the pathogenesis of atherosclerosis.

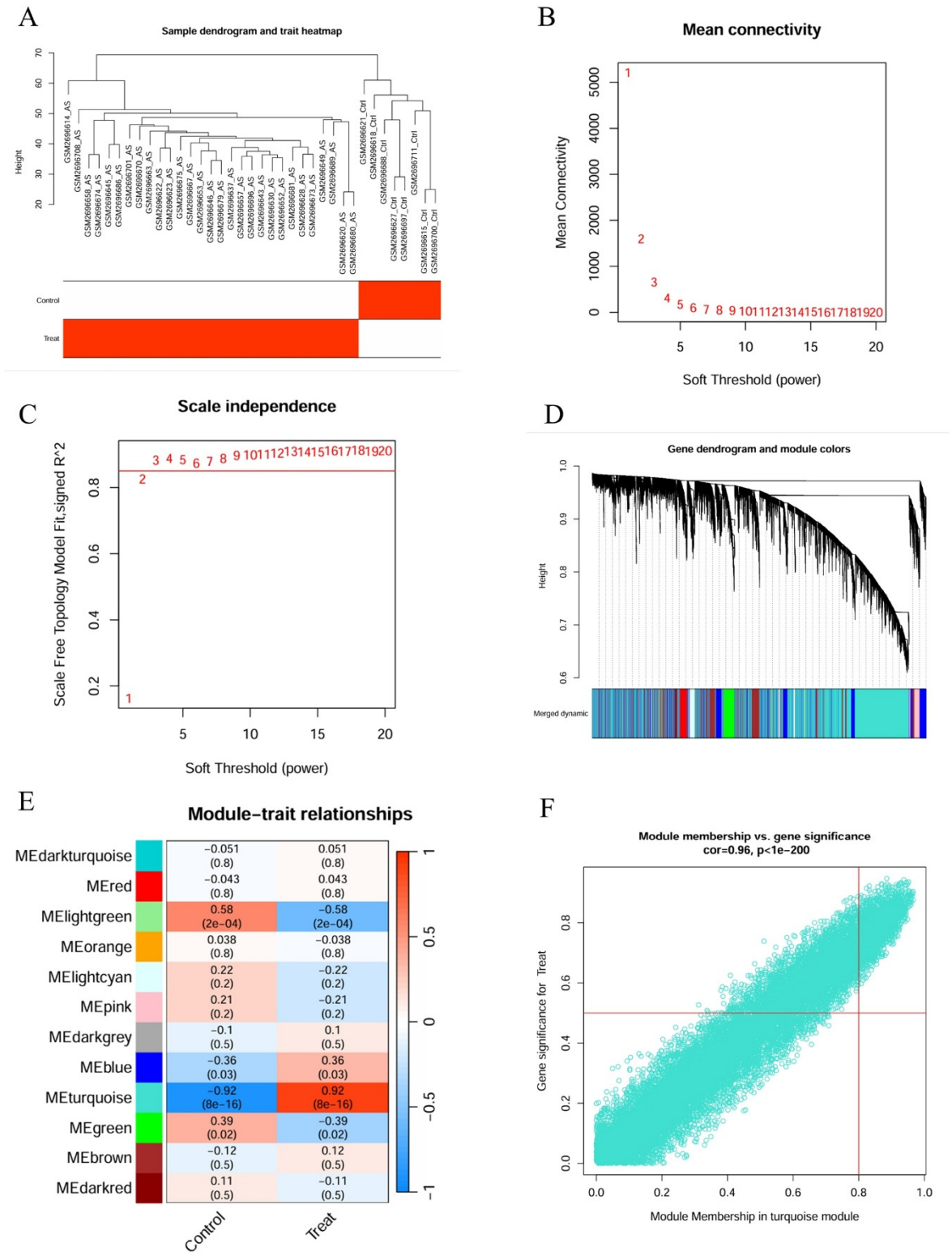

Figure 4. Weighted Gene Co-expression Network Analysis (WGCNA) and Identification of the Key Module Based on the GSE100927 Dataset

(A) Sample clustering dendrogram illustrating the hierarchical clustering of all samples. No significant outliers were detected, indicating reliable data quality. (B) Scale-free topology fit index as a function of the soft-thresholding power (β). β = 9 was selected as the optimal threshold, as the network first satisfied scale-free criteria ($R^2 > 0.9$). (C) Mean connectivity plot under varying soft-threshold values, showing that β = 9 maintains robust network connectivity. (D) Gene dendrogram and module identification based on dynamic tree cutting, with each color representing a distinct gene co-expression module. (E) Heatmap of Pearson correlation coefficients between each module eigengene and the atherosclerosis (AS) phenotype. The turquoise module (MEturquoise) showed the strongest positive correlation with AS (r = 0.92, p = 8e−16). (F) Scatter plot of Module Membership (MM) versus Gene Significance (GS) for genes in the MEturquoise module, demonstrating a strong positive correlation (r = 0.96, $P < 1e{-}200$), indicating key functional relevance of this module to AS pathology.

3.5 Identification of Key Targets of Tiliroside in Atherosclerosis via Multiple Machine Learning Algorithms

To identify the core molecular targets of Tiliroside in the treatment of atherosclerosis (AS), this study integrated three data sources: differentially expressed genes (DEGs), genes from the MEturquoise module identified by WGCNA as significantly associated with AS, and the predicted targets of Tiliroside. The intersection of these datasets yielded seven candidate genes: CCR1, AGTR1, PTGS1, ADRA2C, TNF, CA2, and SYK (Figure 5A). To further refine key targets, three complementary machine learning algorithms were applied for feature selection. First, Least Absolute Shrinkage and Selection Operator (LASSO) regression was performed, with the optimal regularization parameter (λ) determined through cross-validation. This approach identified CCR1, PTGS1, ADRA2C, and SYK as genes with high predictive value (Figures 5B, C). Second, the Random Forest (RF) algorithm was used to evaluate feature importance, highlighting CCR1, AGTR1, PTGS1, and SYK as the most discriminative genes, with the model exhibiting good classification performance and stability (Figures 5D, E). Third, Support Vector Machine–Recursive Feature Elimination (SVM-RFE) was employed, identifying AGTR1, ADRA2C, CCR1, and SYK as the optimal feature set with high accuracy and low error rates (Figure 5F). Among the seven candidates, CCR1 and SYK were consistently selected by all three algorithms, indicating their robust association with the pathogenesis of AS and the therapeutic mechanism of Tiliroside. These two genes were ultimately confirmed as the consensus key targets for subsequent functional validation (Figure 5G).

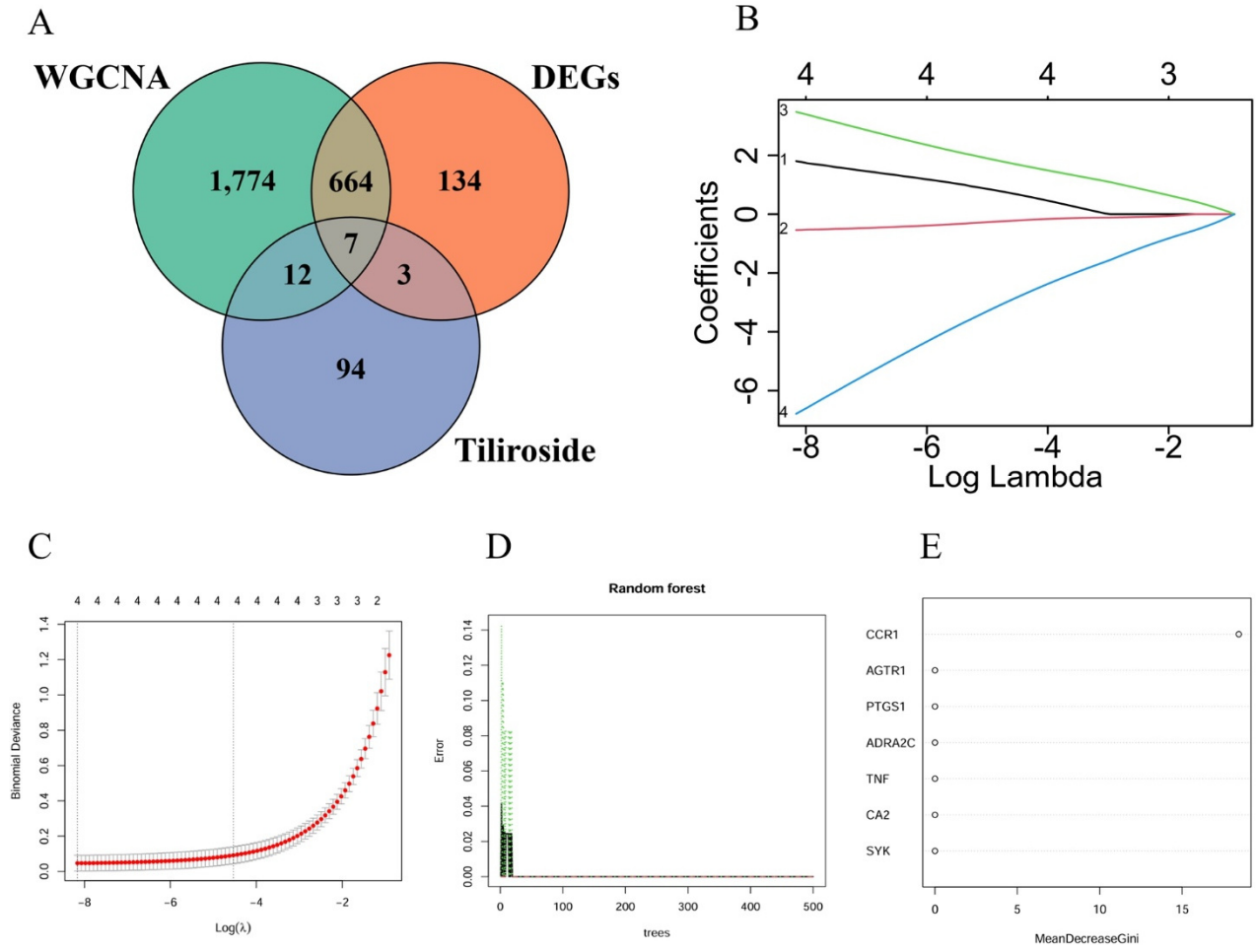

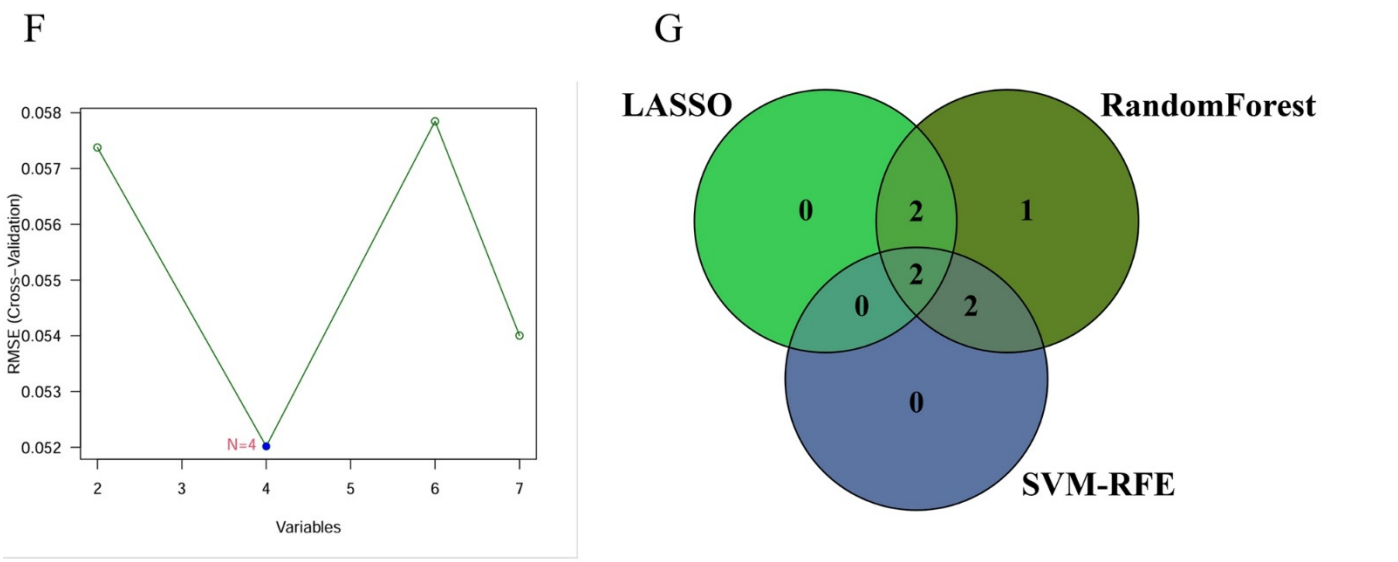

Figure 5. Machine Learning-Based Identification of Core Targets of Tiliroside for Atherosclerosis Intervention
(A) Venn diagram showing the intersection of differentially expressed genes (DEGs), WGCNA-identified MEturquoise module genes, and predicted Tiliroside targets. Seven overlapping candidate genes were identified. (B) LASSO coefficient profiles of the candidate genes as a function of the regularization parameter (λ). (C) Ten-fold cross-validation to determine the optimal λ using the minimum mean squared error criterion, resulting in the selection of four key genes. (D) Error rate plot for the Random Forest (RF) model as the number of decision trees increases, demonstrating convergence and model stability. (E) Variable importance ranking of candidate genes based on the MeanDecreaseGini metric from the RF algorithm. (F) Support Vector Machine–Recursive Feature Elimination (SVM-RFE) analysis identifying the optimal number of features based on root mean square error (RMSE) values. (G) Venn diagram of the selected genes from the three machine learning models (LASSO, RF, and SVM-RFE), with CCR1 and SYK identified as consensus core targets across all methods.

3.6 Immune Infiltration Characteristics in Atherosclerotic Tissues and Immunological Correlation of CCR1 and SYK

To further investigate the immune microenvironment of atherosclerotic (AS) tissues, immune cell infiltration analysis was performed using the CIBERSORT algorithm on transcriptomic data from AS and normal samples (Figures 6A–C). The stacked bar plot revealed a significant enrichment of macrophage subtypes M0, M1, and M2 in AS tissues, with M0 macrophages representing the most abundant infiltrating population (Figure 6A). Violin plot analysis confirmed that the infiltration levels of all three macrophage subtypes were significantly elevated in AS tissues compared to controls (M0: $p = 0.002$; M1: $p = 0.012$; M2: $p = 0.001$), highlighting their potential roles in AS-associated inflammatory responses (Figure 6B). The immune cell Pearson correlation heatmap (Figure 6C) illustrated intricate intercellular interactions. Notably, M0 macrophages exhibited a negative correlation with $CD8^+$ T cells and a positive correlation with regulatory T cells (Tregs) and activated dendritic cells, suggesting a pivotal role for M0 macrophages in shaping the immune co-infiltration landscape. Furthermore, the immunological relevance of the key targets CCR1 and SYK was assessed using the TIMER database. CCR1 expression showed negative correlations with activated dendritic cells, activated $CD4^+$ memory T cells, and M1 macrophages (Figure 6D). In contrast, SYK expression displayed strong negative correlations with $CD8^+$ T cells, Tregs, M1 macrophages, and activated dendritic cells ($p < 0.01$) (Figure 6E). These findings suggest that both CCR1 and SYK may contribute to the regulation of inflammatory responses in AS by modulating immune cell infiltration and activation states within the lesion microenvironment.

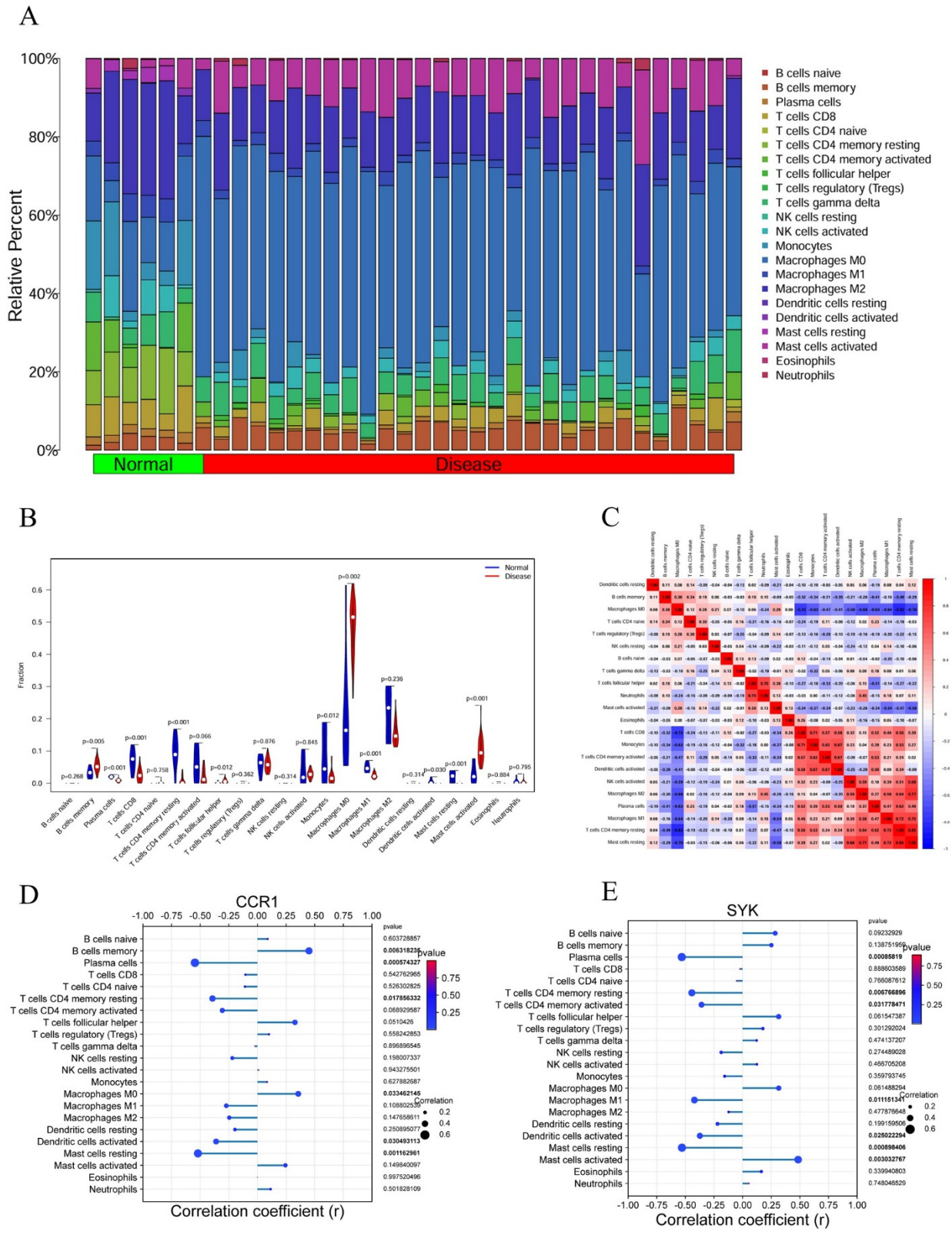

Figure 6. Immune Cell Infiltration in Atherosclerotic Tissues and Correlation Between Key Targets and Immune Cell Populations

(A) Bar chart showing the estimated proportions of 22 immune cell types in AS and normal control tissues using the CIBERSORT algorithm. (B) Violin plots displaying the distribution differences in immune cell infiltration between groups. Macrophages M0, M1, M2, regulatory T cells (Tregs), activated dendritic cells, and eosinophils were significantly elevated in AS, whereas memory B cells, resting memory CD4+ T cells, and CD8+ T cells were reduced. (C) Pearson correlation heatmap indicating potential co-infiltration or antagonistic relationships among immune cell subsets. (D–E) Correlation analysis using the TIMER database. Expression levels of CCR1 (D) and SYK (E) were correlated with the degree of infiltration of various immune cell types in AS tissues.

3.7 Expression Characteristics of CCR1 and SYK in Atherosclerotic Tissues and Tiliroside–SYK Molecular Interaction and Stability Analysis

To further validate the expression profiles of CCR1 and SYK in atherosclerotic (AS) tissues, transcriptomic data from the GEO dataset GSE43292 were analyzed. Both CCR1 and SYK were significantly upregulated in AS samples compared to normal controls, with strong statistical significance (CCR1: $p = 2.5 \times 10^{-7}$; SYK: $p = 5.5 \times 10^{-7}$) (Figures S7A–B). To assess their diagnostic potential, Receiver Operating Characteristic (ROC) curve analysis was performed. The area under the curve (AUC) for CCR1 was 0.854 (95% CI: 0.753–0.940), and for SYK, it was 0.845 (95% CI: 0.744–0.933), indicating robust discriminatory power for distinguishing AS from control tissues (Figures S7C–D).To explore the molecular interactions of Tiliroside with the two targets, molecular docking was conducted (Figure 7A). Tiliroside displayed a binding energy of −7.513 kcal/mol with SYK and −4.66 kcal/mol with CCR1. Since a binding energy below −5.0 kcal/mol typically indicates strong binding potential, the interaction between Tiliroside and CCR1 was considered relatively weak. In contrast, Tiliroside exhibited stronger affinity for SYK, suggesting a more stable binding conformation and higher likelihood of biological activity. Further conformational analysis revealed that Tiliroside forms a stable interaction network with SYK, involving hydrogen bonds, π–π stacking, and salt bridges with key residues such as Glu205, Tyr347, Cys51, Asp345, and Phe357. A two-dimensional interaction diagram confirmed multiple polar, charged, and aromatic residue interactions, supporting the structural stability of the Tiliroside–SYK complex. To evaluate the dynamic stability of the complex, a 100 ns molecular dynamics (MD) simulation was performed. The results were as follows:

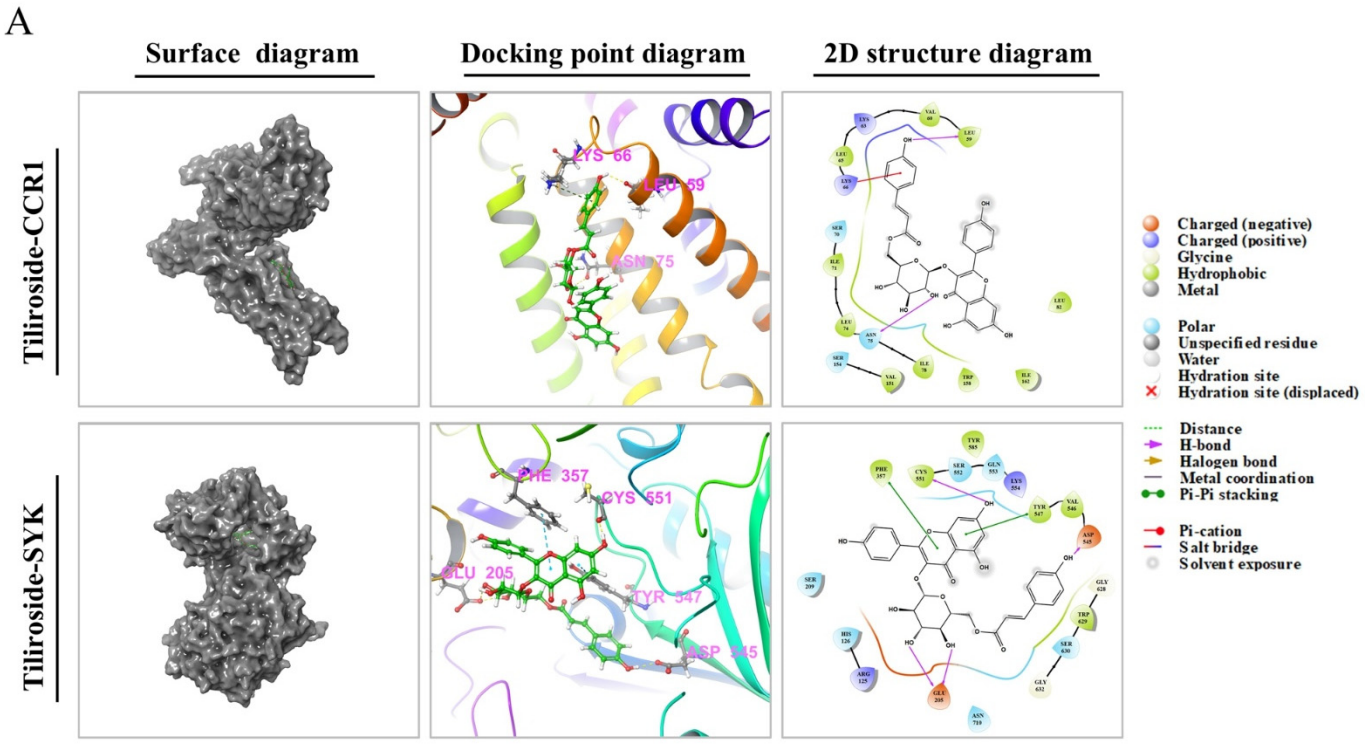

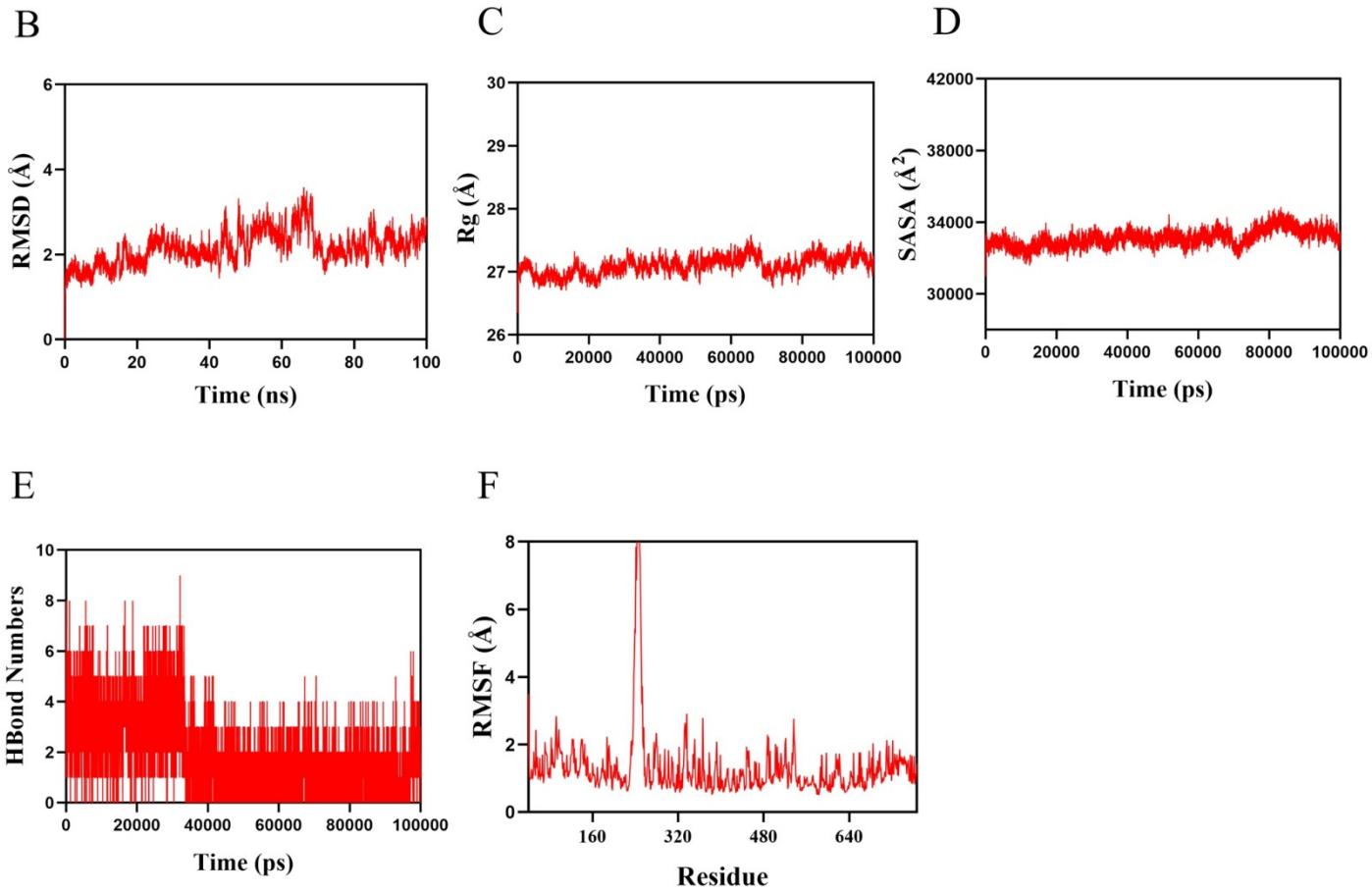

Figure 7. Molecular Docking and Molecular Dynamics Simulation of Tiliroside with Target Proteins CCR1 and SYK (A) Docking conformations of Tiliroside with CCR1 (top row) and SYK (bottom row). (B) Root Mean Square Deviation (RMSD) analysis showing that the Tiliroside–SYK complex reached equilibrium around 70 ns, with RMSD fluctuations stabilized at approximately 2.8 Å, indicating structural stability. (C) Radius of Gyration (Rg) analysis demonstrating that the overall compactness of the SYK structure remained consistent throughout the simulation. (D) Solvent Accessible Surface Area (SASA) profile showing minimal changes in surface exposure, indicating that Tiliroside binding did not significantly alter the overall protein conformation. (E) Hydrogen bond analysis showing that the Tiliroside–SYK complex consistently maintained approximately four stable hydrogen bonds during the 100 ns simulation. (F) Root Mean Square Fluctuation (RMSF) analysis revealing low conformational flexibility for most residues, with only minor fluctuations in localized regions, supporting the structural rigidity of the complex.

RMSD analysis (Figure 7B): The complex reached equilibrium after ~70 ns, maintaining stable conformation fluctuations at ~2.8 Å.

Radius of Gyration (Rg) (Figure 7C): The complex remained compact throughout the simulation, with an average Rg of ~27.0 Å.

Solvent Accessible Surface Area (SASA) (Figure 7D): The surface area fluctuated stably between 33,000–36,000 Å², with no evidence of significant unfolding.

Hydrogen bond analysis (Figure 7E): On average, four hydrogen bonds were consistently maintained between the ligand and protein, contributing to interaction stability.

RMSF analysis (Figure 7F): Residue flexibility remained low across most regions, with fluctuations generally below 2.3 Å, indicating limited conformational variation.

Collectively, these results suggest that SYK is not only significantly overexpressed in AS tissues and exhibits strong diagnostic potential, but also binds Tiliroside with high affinity and structural stability. Therefore, SYK was selected as the primary molecular target for subsequent functional validation studies.

3.8 Single-Cell Transcriptomic Analysis Reveals Cell-Specific Expression Pattern of SYK in Atherosclerotic Tissues

To identify the specific cell types expressing SYK in atherosclerotic (AS) lesions, a single-cell transcriptomic analysis was performed using the publicly available dataset GSE159677 from the GEO database. The aim was to characterize cellular composition changes and determine the cell-specific expression profile of SYK in AS tissues. Following standard preprocessing steps—including quality control, normalization, dimensionality reduction, and clustering—UMAP visualization (Figure 8A) identified eight major cell populations: T cells, B cells, monocytes, macrophages, fibroblasts, endothelial cells, smooth muscle cells (SMCs), and mast cells. These clusters showed clear boundaries and well-resolved heterogeneity, confirming reliable cell-type identification. SYK expression analysis across these clusters (Figure 8B) revealed high expression levels in monocytes and macrophages, whereas its expression in T cells, endothelial cells, and other non-myeloid cells remained relatively low. This suggests that SYK predominantly functions in myeloid-derived immune responses. Further comparative analysis between AS and control samples (Figures 8C – E) showed that the macrophage proportion was significantly elevated in AS tissues, and SYK expression was markedly upregulated within this population. These findings imply that SYK may play a crucial regulatory role in immune activation and inflammatory microenvironment remodeling associated with AS. Additionally, heatmap analysis of the top five marker genes for each cell cluster (Figure S8A) validated the accuracy of cell-type annotations. Monocyte clusters highly expressed canonical myeloid markers LYZ and FCN1; macrophage clusters were enriched for complement-related genes C1QA, C1QB, and C1QC; T cells expressed classical immune activation genes CCL5 and IL7R; and SMCs exhibited high levels of contractile protein genes ACTA2, TAGLN, and MYL9. In conclusion, single-cell transcriptomic profiling highlighted substantial immune cell infiltrationin AS lesions and confirmed that SYK is highly expressed in myeloid immune cells, especially macrophages. Based on these results, macrophages were selected as the primary cellular target for subsequent in vivo and in vitro functional validation experiments on SYK in atherosclerosis.

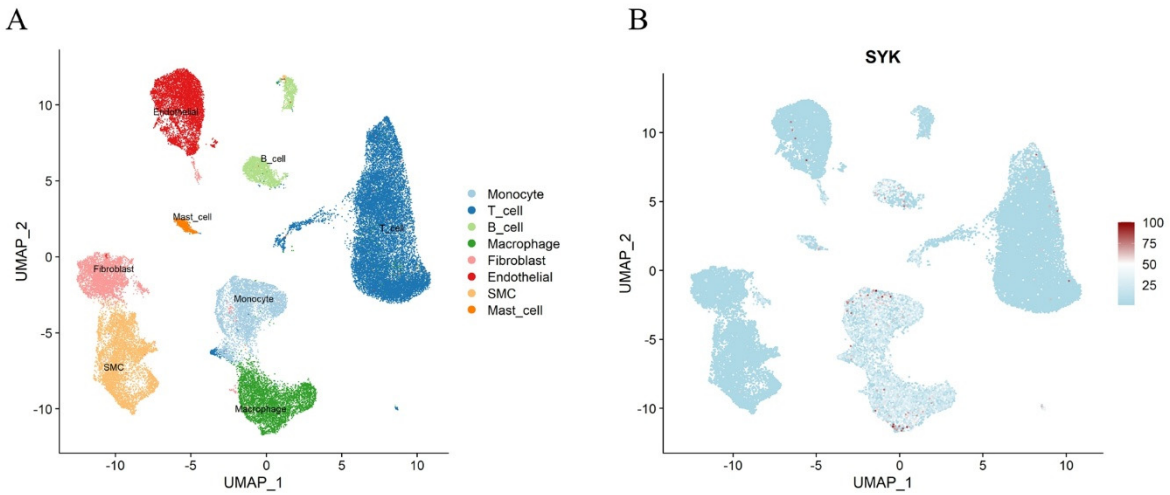

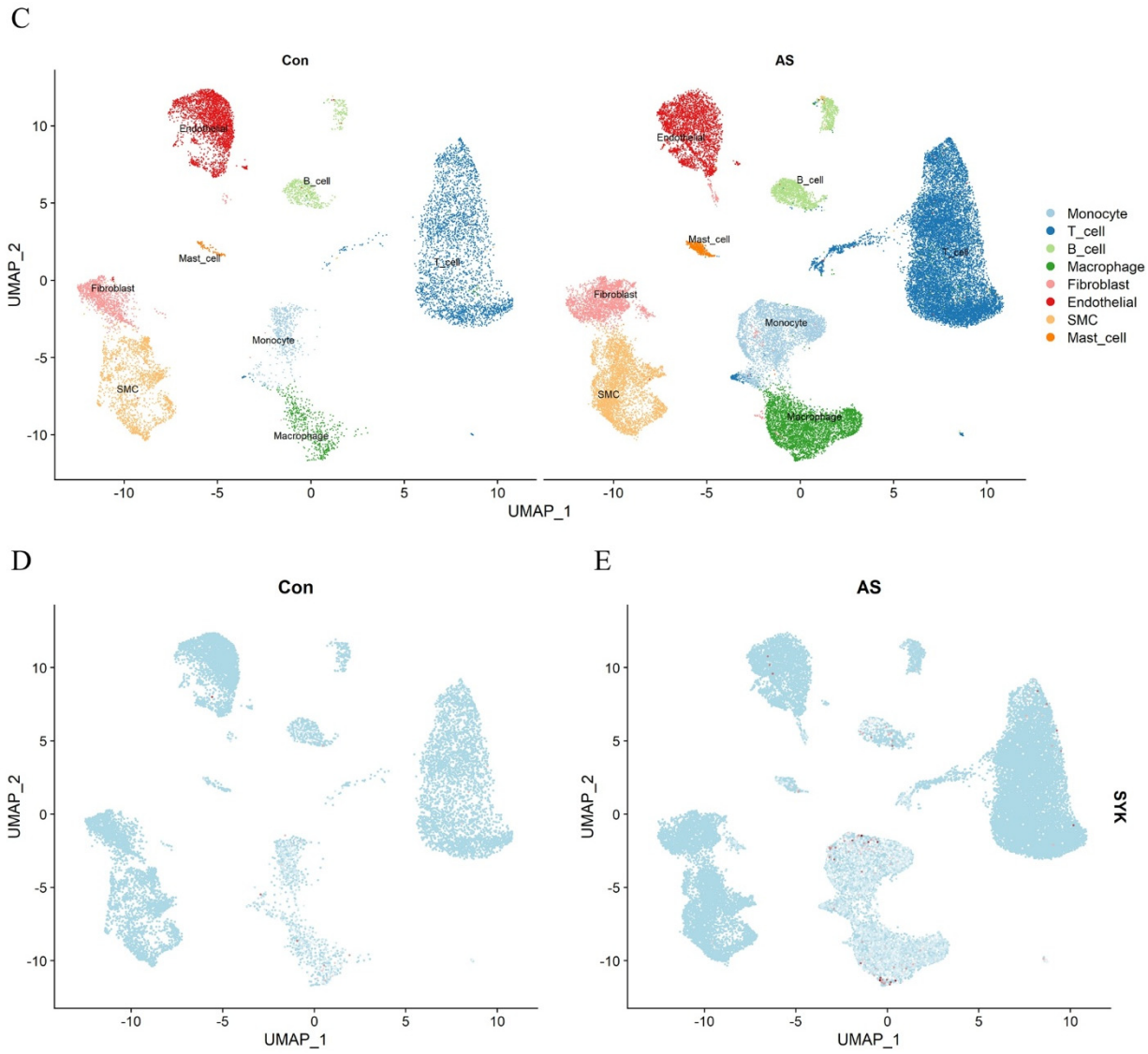

Figure 8. Single-Cell Transcriptomic Profiling of SYK Expression in Atherosclerotic Lesions

(A) UMAP plot depicting the clustering of single-cell populations from AS tissue, identifying eight major cell types: T cells, B cells, monocytes, macrophages, fibroblasts, endothelial cells, smooth muscle cells (SMCs), and mast cells. (B) Cell-type-specific expression analysis of SYK, showing predominant expression in monocytes and macrophages. (C) Comparison of macrophage proportions between AS and control (Con) tissues, revealing a marked increase in macrophages in AS samples. (D) Expression analysis of SYK in macrophages from AS and control tissues, indicating significant upregulation in the AS group. (E) SYK expression dynamics in the macrophage population, illustrating its key role in myeloid cell activation during AS progression.

3.9 Tiliroside Promotes Cholesterol Efflux and Inhibits Foam Cell Formation

To investigate the regulatory effect of Tiliroside on foam cell formation in macrophages, an ox-LDL-induced RAW264.7 macrophage foam cell model was established. First, CCK-8 assay results indicated that Tiliroside treatment at concentrations of 10, 20, and 40 μmol/L maintained RAW264.7 cell viability above 90% (Figure S9A), suggesting no significant cytotoxicity within the tested concentration range. Oil Red O staining demonstrated that ox-LDL treatment significantly induced lipid droplet accumulation and extensive foam cell formation, whereas Tiliroside treatment markedly reduced lipid accumulation in a dose-dependent manner (Figure 9A). Subsequent lipid quantification further confirmed that Tiliroside significantly decreased the intracellular levels of total lipids (Figure 9B), total cholesterol

(Figure 9C), free cholesterol (Figure 9D), and cholesteryl esters (Figure 9E), indicating its effective inhibition of foam cell formation. Foam cell formation is mainly governed by three metabolic pathways: lipid uptake, cholesterol esterification, and cholesterol efflux[53, 54]. To identify the regulatory target of Tiliroside, the expression of key genes in these pathways was assessed. The results showed that Tiliroside had no significant effect on lipid uptake receptors (CD36, SR-A, and LOX-1) or cholesterol esterification-related enzymes (NCEH1 and ACAT-1) (Figures S9B–F), suggesting that its anti-foam cell effect does not operate via these pathways. Importantly, Tiliroside significantly upregulated the mRNA expression of the cholesterol efflux transporters ABCA1 (Figure 9F) and ABCG1 (Figure 9G). Cholesterol efflux assays further validated that Tiliroside markedly enhanced the transport of cholesterol to HDL and ApoA-I (Figures 9H–I), thereby reducing intracellular cholesterol accumulation. At the protein level, Western blot analysis showed a dose-dependent increase in ABCA1 (Figure 9J) and ABCG1 (Figure 9K) expression, with the 40 μmol/L group exhibiting the most pronounced effect. Quantitative grayscale analysis confirmed that the upregulation was statistically significant (Figures 9L–M). In summary, Tiliroside significantly inhibits ox-LDL-induced foam cell formation by enhancing cholesterol efflux rather than affecting lipid uptake or esterification. This effect is mediated through the upregulation of ABCA1 and ABCG1, which play a key role in facilitating intracellular cholesterol removal and mitigating lipid accumulation.

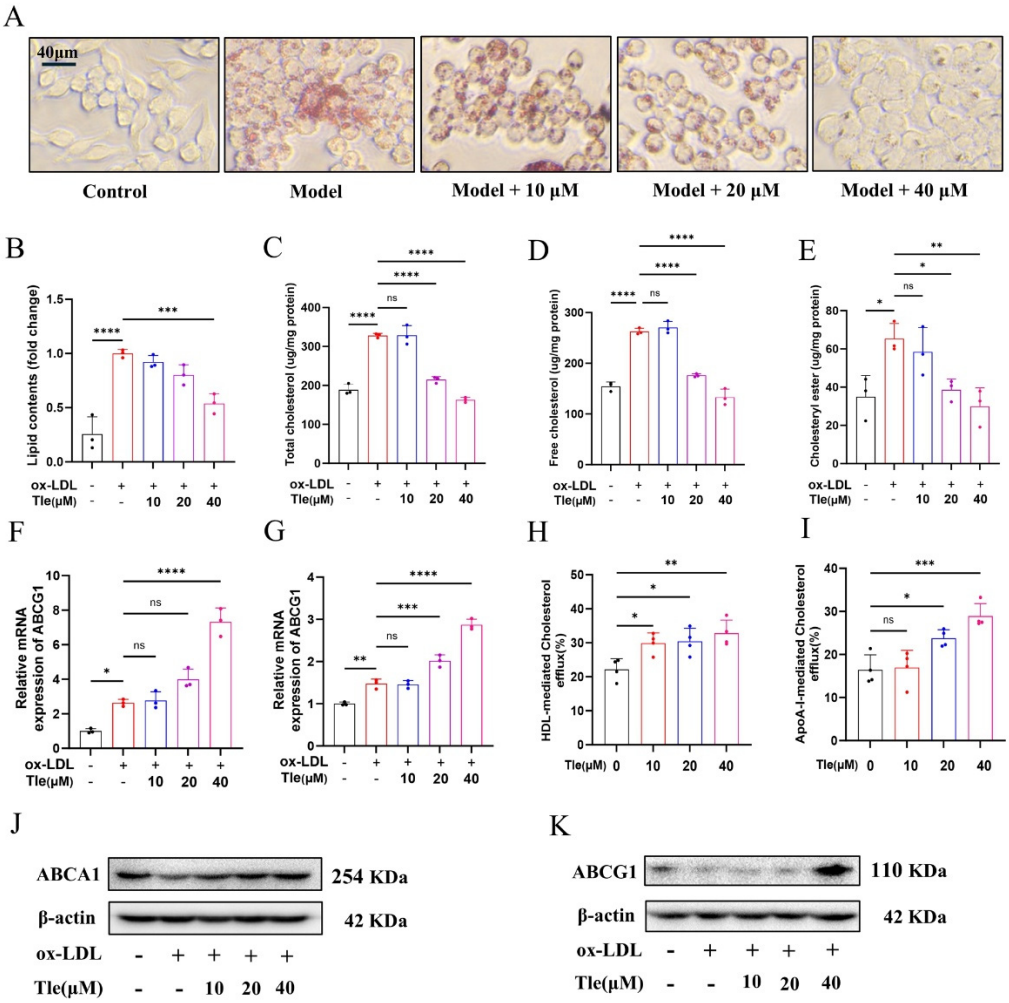

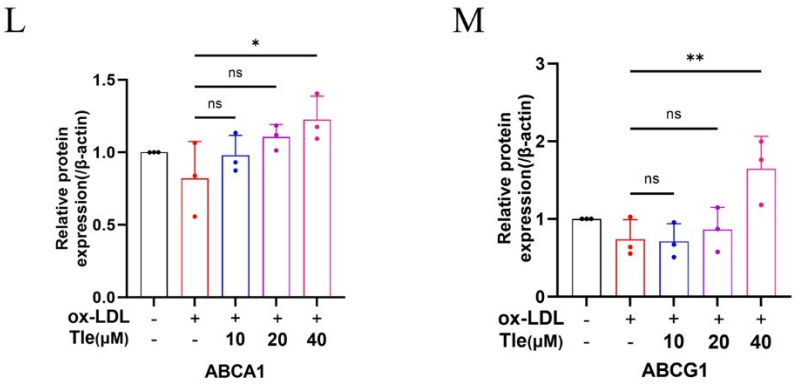

Figure 9. Tiliroside Inhibits Ox-LDL–Induced Foam Cell Formation in RAW264.7 Macrophages
(A) Representative Oil Red O staining images demonstrating intracellular lipid accumulation in different treatment groups. (B) Quantitative analysis of Oil Red O–positive lipid areas, indicating reduced lipid deposition following Tiliroside treatment. (C–E) Intracellular cholesterol quantification. (F–G) Quantitative real-time PCR results showing upregulation of cholesterol efflux transporters: ABCA1 mRNA expression (F), ABCG1 mRNA expression (G). (H–I) Cholesterol efflux assays showing that Tiliroside significantly enhances cholesterol transport to: HDL (H), ApoA-I (I). (J–K) Western blot analysis showing dose-dependent increases in protein expression of: ABCA1 (J), ABCG1 (K). (L–M) Densitometric quantification of ABCA1 (L) and ABCG1 (M) protein expression levels. Data are presented as mean ± standard deviation (SD); statistical significance is indicated as $^{*}P < 0.05$, $^{**}P < 0.01$, $^{***}P < 0.001$, $^{***}P < 0.0001$.

3.10 In Vivo and In Vitro Validation of SYK as the Key Target for Tiliroside's Anti-Atherosclerotic Effect

To validate whether SYK serves as a key target mediating the anti-atherosclerotic effects of Tiliroside, we first assessed its activation status in macrophage-derived foam cells. Western blot analysis revealed that phosphorylated SYK (p-SYK) levels increased rapidly within 0.5 hours of ox-LDL stimulation, followed by a gradual decline (Figure 10A), indicating that SYK is activated during the early phase of foam cell formation. Consequently, a 0.5-hour ox-LDL stimulation was selected as the intervention time point for subsequent experiments. Under this condition, Tiliroside treatment did not affect total SYK protein expression, but dose-dependently suppressed the upregulation of p-SYK (Figure 10B). Densitometric analysis further confirmed a significant reduction in the p-SYK/SYK ratio (Figure 10E), suggesting that Tiliroside effectively inhibits SYK phosphorylation and activation. To verify whether this regulatory effect also occurs in vivo, we examined p-SYK expression in macrophages within aortic lesion tissues from ApoE$^{-/-}$ atherosclerotic mice using immunofluorescence staining. The results showed a marked increase in p-SYK signal within CD68-positive macrophage regions in the model group, indicating active SYK signaling at the lesion site. In contrast, the high-dose Tiliroside group (H-Tle) exhibited notably reduced p-SYK fluorescence intensity and diminished co-localization with CD68 (Figures 10C–D), indicating that Tiliroside effectively inhibits macrophage SYK activation in vivo. Given that SYK activation mediates several pro-inflammatory signaling pathways, including NF-κB, and promotes the expression of inflammatory cytokines such as IL-6, TNF-α, and IL-1β, we further analyzed the expression levels of these markers[55, 56]. The results demonstrated that Tiliroside significantly inhibited both mRNA and protein expression of IL-6, TNF-α, and IL-1β induced by ox-LDL (Figures 10F–H; Figures S10A–C), indicating that its anti-inflammatory effects are closely linked to suppression of SYK signaling. Additionally, ROS staining (Figure 10I) revealed that ox-LDL stimulation significantly increased intracellular reactive oxygen species (ROS) levels, while Tiliroside dose-dependently reduced ROS

accumulation. This suggests that its anti-inflammatory mechanism may also involve attenuation of oxidative stress.

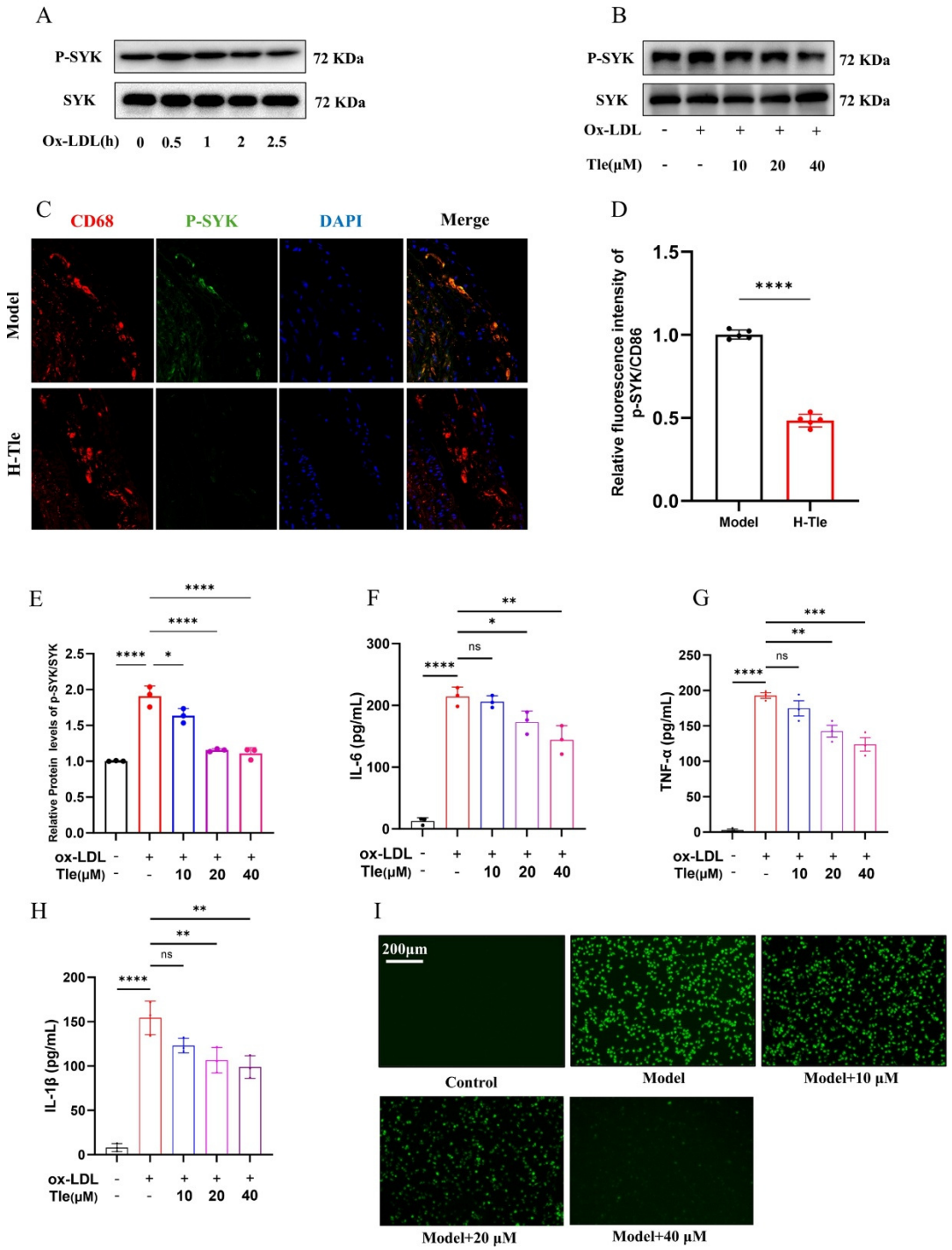

Figure 10. Tiliroside Inhibits SYK Phosphorylation and Downstream Inflammatory Signaling Pathways
(A) Western blot analysis of phosphorylated SYK (p-SYK) levels at various time points (0–2.5 h) following ox-LDL stimulation in RAW264.7 macrophages, showing early activation of SYK. (B) Western blot results showing that Tiliroside dose-dependently suppresses p-SYK expression without affecting total SYK levels. (C) Immunofluorescence staining of mouse aortic tissue, revealing p-SYK expression within CD68-positive macrophage regions. (D) Quantitative analysis of fluorescence intensity indicating a significant reduction in p-SYK signal in the high-dose Tiliroside treatment group, demonstrating in vivo suppression of SYK activation. (E) Densitometric analysis showing a significant decrease in the p-SYK/SYK ratio following Tiliroside intervention. (F–H) ELISA results showing that Tiliroside significantly inhibits the LPS-induced production of pro-inflammatory cytokines IL-6 (F), TNF-α (G), and IL-1β (H), confirming its anti-inflammatory effect. (I) ROS staining results demonstrating that Tiliroside dose-dependently reduces intracellular reactive oxygen species (ROS) accumulation induced by LPS. *Data are expressed as mean ± standard deviation (SD); $^{*}P < 0.05$, $^{**}P < 0.01$, $^{***}P <$ 0.001, ***0.0001.

3.11 Tiliroside's Regulation of Lipid Metabolism and Inflammatory Factors Depends on SYK Expression

To determine whether the regulatory effects of Tiliroside on lipid metabolism and inflammation are dependent on SYK expression, small interfering RNA (siRNA) was used to knock down SYK, followed by functional validation. The CCK-8 assay confirmed that siRNA transfection did not significantly affect the viability of RAW264.7 cells (Figure 11K), excluding cytotoxic effects as a confounding factor. qPCR and Western blot results demonstrated that both siRNA-SYK1 and siRNA-SYK2 effectively silenced SYK expression, with siRNA-SYK2 showing greater knockdown efficiency and thus selected for subsequent experiments (Figures 11A – C). In the foam cell model, ox-LDL stimulation induced marked lipid droplet accumulation, whereas Tiliroside treatment significantly reduced intracellular lipid deposition (Figure 11D). However, upon SYK silencing, the lipid-lowering effect of Tiliroside was substantially attenuated (Figure 11E), indicating that its inhibition of foam cell formation is SYK-dependent. Further cholesterol efflux assays revealed that under normal conditions (NC), Tiliroside significantly enhanced cholesterol efflux to HDL and ApoA-I (Figures 11F – G). However, this promoting effect was markedly weakened after SYK knockdown, suggesting that Tiliroside's effect on cholesterol transport also relies on SYK signaling. In the foam cell model, ELISA assays showed that Tiliroside significantly inhibited the secretion of pro-inflammatory cytokines IL-6, TNF-α, and IL-1β (Figures 11H – J). Yet, after SYK silencing, the anti-inflammatory effect was significantly reduced, further confirming that the integrity of the SYK pathway is essential for Tiliroside's immunomodulatory activity. In conclusion, both in vitro and in vivo experiments demonstrated that SYK is a critical molecular target mediating the anti-atherosclerotic effects of Tiliroside. By inhibiting SYK phosphorylation and activation, Tiliroside modulates inflammatory signaling and oxidative stress responses, thereby alleviating lipid accumulation and inflammation in atherosclerosis.

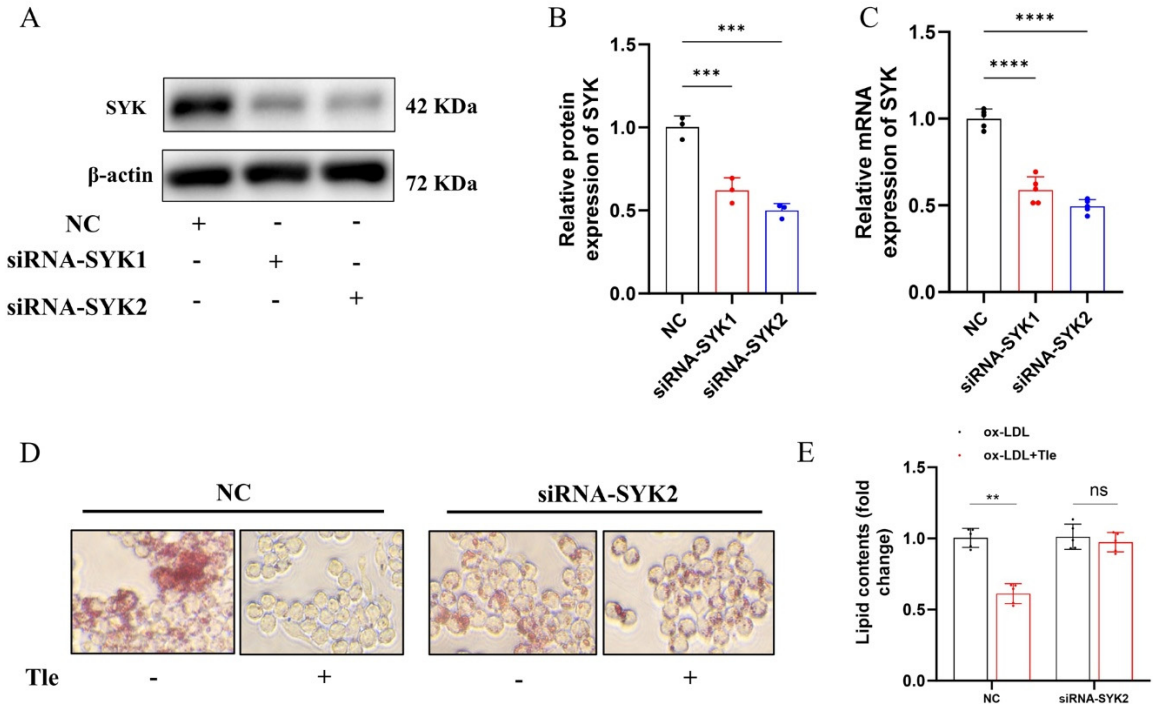

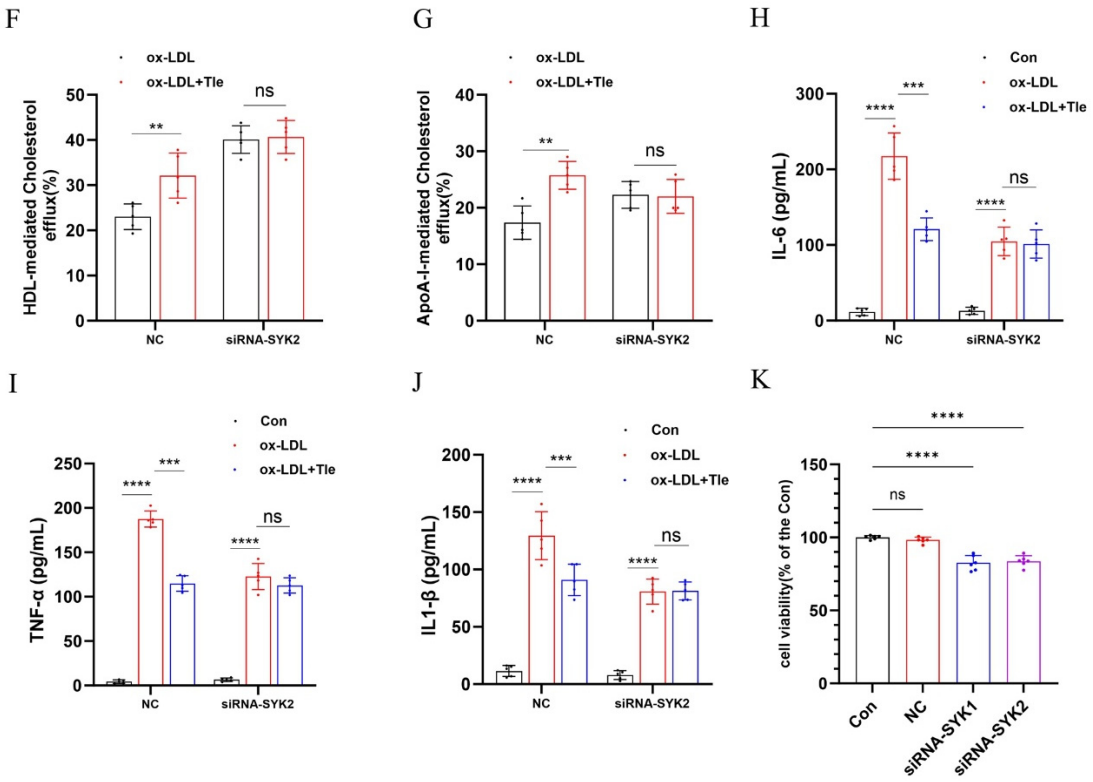

Figure 11. Tiliroside Regulates Lipid Accumulation and Inflammatory Responses in RAW264.7 Macrophages via SYK Inhibition

(A–C) qPCR and Western blot analyses showing that siRNA-SYK1 and siRNA-SYK2 effectively suppress SYK expression at both the mRNA and protein levels in RAW264.7 cells. siRNA-SYK2 exhibited superior silencing efficiency and was selected for subsequent validation experiments. (D) Representative Oil Red O staining images of foam cells showing ox-LDL–induced lipid droplet accumulation and the lipid-lowering effect of Tiliroside. (E) Quantitative lipid analysis demonstrating that SYK knockdown significantly weakens Tiliroside's effect in reducing intracellular lipid accumulation, indicating a SYK-dependent mechanism. (F–G) Cholesterol efflux assays showing that Tiliroside enhances HDL- and ApoA-I–mediated cholesterol efflux under normal conditions; however, this effect is markedly attenuated after SYK silencing. (H–J) ELISA results showing that Tiliroside significantly reduces the LPS-induced secretion of IL-6 (H), TNF-α (I), and IL-1β (J); this anti-inflammatory effect is significantly diminished in SYK-deficient cells. (K) CCK-8 assay results showing that siRNA transfection does not compromise RAW264.7 cell viability, excluding cytotoxic interference. Statistical analysis: compared with the corresponding control group, $^{*}P < 0.05$, $^{**}P < 0.01$, $^{***}P < 0.001$, $^{***}P < 0.0001$; ns = not significant.

4. Conclusion and Discussion

This study systematically evaluated the therapeutic potential of the natural flavonoid Tiliroside in AS and elucidated its mechanisms of action across multiple dimensions, including molecular networks, immune regulation, and cellular function. Animal experiments demonstrated that Tiliroside markedly attenuated plaque progression, improved lipid metabolism, and reduced lesion burden in ApoE$^{-/-}$ mice. Through integrated multi-omics analysis combined with machine learning, spleen tyrosine kinase (SYK) was identified as the core molecular target. Molecular docking and molecular dynamics simulations confirmed a strong and stable interaction between Tiliroside and SYK. Immune infiltration and single-cell transcriptomic analyses further revealed SYK-specific overexpression in macrophages within AS lesions. Functional validation in vitro and in vivo demonstrated that Tiliroside inhibited SYK phosphorylation and activation, promoted cholesterol efflux, suppressed foam cell formation, and reduced the secretion of pro-inflammatory cytokines (IL-6, TNF-α, and IL-1β). Moreover, siRNA-mediated SYK knockdown confirmed the SYK dependency of

these effects. Collectively, this study provides the first evidence that the "Tiliroside–SYK–macrophage" axis plays a central role in mediating the anti-atherosclerotic actions of Tiliroside. Previous studies have mainly highlighted the anti-inflammatory activity of Tiliroside in acute inflammation models, such as acute kidney injury, acute lung injury, and ulcerative colitis[57-60]. More recent evidence indicates that Tiliroside may also ameliorate myocardial ischemic injury by modulating PI3K–Akt and MAPK signaling pathways, suggesting broader cardiovascular benefits[61]. However, systematic investigations into its roles in chronic inflammatory diseases such as AS, particularly regarding immune regulation, have been lacking. The present study fills this gap by linking Tiliroside's pharmacological effects to the immune–metabolic network in AS, revealing a dual regulatory mechanism: (1) upregulating ABCA1 and ABCG1 to enhance cholesterol efflux, and (2) directly suppressing SYK activation to mitigate inflammatory responses.

As a non-receptor tyrosine kinase, spleen tyrosine kinase (SYK) serves as a central signaling hub in various immune–metabolic disorders[62]. In rheumatoid arthritis, SYK mediates Fcγ receptor (FcγR) signaling, promotes the production of pro-inflammatory cytokines such as TNF-α and IL-6, and facilitates Th17 cell differentiation via the PI3K/AKT/mTOR pathway[63-65]. SYK also plays a crucial role in the pathogenesis of systemic lupus erythematosus (SLE), particularly in lupus nephritis[66, 67]. Anti-phosphatidylserine antibodies produced by B1 cells have been shown to activate SYK through Toll-like receptor (TLR)-mediated signaling, thereby amplifying inflammatory responses and accelerating renal injury[68]. In addition, SYK promotes immune dysregulation by enhancing antigen presentation in glomerular podocytes, which leads to increased T cell activation. Pharmacological inhibition of SYK with GS-9973 effectively blocks podocyte-mediated antigen presentation and suppresses T cell activation, thereby alleviating lupus nephritis induced by the knockdown of signal regulatory protein alpha (SIRPα)[69]. These findings highlight the therapeutic potential of SYK inhibition in SLE-associated renal pathology. In the context of non-alcoholic steatohepatitis (NASH), SYK plays a pivotal regulatory role in orchestrating hepatic inflammation and fibrogenesis. Recent evidence demonstrates that CYR61 activates the IRAK4/SYK/NF-κB signaling cascade, promoting the polarization of hepatic monocytes toward a pro-inflammatory and pro-fibrotic phenotype. This activation leads to the upregulation of fibrogenic mediators such as PDGFa and PDGFb in macrophages, thereby exacerbating liver inflammation and fibrosis[70]. Furthermore, SYK enhances the activation of hematopoietic stem cells by upregulating specific transcription factors, thus further accelerating hepatic fibrogenesis[71]. Similarly, in inflammatory bowel disease (IBD), fungal dysbiosis has been shown to activate the Dectin-1/SYK/NF-κB pathway, resulting in the upregulation of enzymes and transporters involved in glutamine metabolism, thereby contributing to intestinal inflammation and disease progression[72]. Targeted delivery of SYK inhibitors via CCL4-modified nanoparticles has demonstrated efficacy in mitigating IBD-associated inflammation[73]. Moreover, Tanshinone I alleviates dextran sulfate sodium (DSS)-induced colitis by inhibiting SYK-mediated inflammasome activation and suppressing macrophage-driven inflammation[74]. Collectively, these findings underscore SYK as a convergent therapeutic target across diverse immune–metabolic diseases. The inhibitory effects of compounds such as Tiliroside on SYK may thus hold broad therapeutic potential beyond AS.

Although SYK was established as a direct molecular target, Tiliroside's effects are unlikely to be mediated by a single pathway. The observed upregulation of ABCA1 and ABCG1 aligns with the liver X receptor (LXR) signaling axis. For instance, Soraphen A enhances cholesterol efflux in THP-1–derived foam cells via LXR-mediated ABCA1 induction[75]. Chitosan oligosaccharides activate PPAR-γ/LXR-α signaling and induce AMPK phosphorylation to stimulate ABCA1/ABCG1-dependent efflux; and the traditional formulation Yin-xing-tong-mai decoction has been shown to activate the PPARγ/LXRα pathway, upregulate ABCA1/ABCG1, enhance cholesterol efflux, and attenuate AS in mice[76, 77]. These findings, consistent with our observations, suggest that Tiliroside may directly or indirectly activate LXR signaling, synergizing with SYK inhibition. In addition, Tiliroside has been reported to modulate PI3K–Akt, MAPK, and NF-κB pathways, which are intimately linked with macrophage polarization, cytokine transcription, and cholesterol metabolism[78-80]. Thus, Tiliroside's anti-atherosclerotic effects likely arise from a multi-target, multi-pathway synergy: directly suppressing SYK-mediated inflammatory signaling while simultaneously engaging nuclear receptor and inflammatory signaling networks (LXR/PPARγ/AMPK, PI3K–Akt, MAPK, and NF-κB) to promote cholesterol efflux and attenuate inflammation.

Despite providing systematic evidence, this study has several limitations. ApoE$^{-/-}$ mice develop lipid-rich plaques rapidly under high-fat feeding, whereas human AS progresses more slowly and involves more complex inflammatory, fibrotic, and calcific remodeling. Similarly, RAW264.7 macrophages, as immortalized murine cells, differ in gene expression and functional states from human macrophages, which may limit translational relevance. Therefore, future studies should: (1) employ more clinically representative AS models, such as LDLR$^{-/-}$ mice, ApoE$^{-/-}$ models with metabolic comorbidities, or humanized models, to better capture human disease heterogeneity; (2) validate SYK's role in human-derived macrophages and PBMCs, potentially incorporating CRISPR/Cas9 editing to strengthen causal inference and cross-species applicability; (3) develop targeted delivery strategies for Tiliroside, such as nanoparticle-based formulations or antibody-conjugated carriers, to improve bioavailability, tissue specificity, and therapeutic index; and (4) construct integrated immune–metabolism–signaling models and apply single-cell and spatial transcriptomics to dissect the vascular microenvironment under Tiliroside treatment, thereby advancing the development of precision immunometabolic therapies.

In conclusion, this study provides the first evidence that the "Tiliroside–SYK–macrophage" axis constitutes a central mechanism underlying the anti-atherosclerotic effects of Tiliroside. By simultaneously suppressing SYK-mediated inflammatory signaling and enhancing cholesterol efflux, Tiliroside effectively reduces foam cell formation and vascular inflammation. These findings not only provide new mechanistic insights into the pharmacological actions of natural products in AS but also establish SYK as a promising immunometabolic therapeutic target for future translational applications.

Ethical Compliance for Public Database Data

The transcriptomic datasets used in this study were obtained from the Gene Expression Omnibus (GEO), a publicly accessible repository. All original studies associated with these datasets received ethical

approval, and participants provided written informed consent. As these data are publicly available, researchers are permitted to download and utilize them for secondary analysis and publication in accordance with established ethical guidelines for public data use.

Data Availability Statement

All data generated or analyzed during this study are included in the published article and its supplementary materials. For further inquiries, please contact the corresponding author. The publicly available transcriptomic datasets used in this study can be accessed through the GEO database under accession numbers GSE100927 and GSE159677.

Conflicts of Interest

The authors declare no competing financial interests or personal relationships that could have influenced the findings presented in this work.

References

[1] G.A. Roth, G.A. Mensah, C.O. Johnson, et al., Global Burden of Cardiovascular Diseases and Risk Factors, 1990-2019: Update From the GBD 2019 Study, J Am Coll Cardiol. 76 (2020) 2982-3021. https://doi.org/10.1016/j.jacc.2020.11.010.

[2] Global burden of 87 risk factors in 204 countries and territories, 1990-2019: a systematic analysis for the Global Burden of Disease Study 2019, Lancet. 396 (2020) 1223-1249. https://doi.org/10.1016/s0140-6736(20)30752-2.

[3] S. Jebari-Benslaiman, U. Galicia-García, A. Larrea-Sebal, et al., Pathophysiology of Atherosclerosis, Int J Mol Sci. 23 (2022) https://doi.org/10.3390/ijms23063346.

[4] J. Wang, Q. Wu, X. Wang, et al., Targeting Macrophage Phenotypes and Metabolism as Novel Therapeutic Approaches in Atherosclerosis and Related Cardiovascular Diseases, Curr Atheroscler Rep. 26 (2024) 573-588. https://doi.org/10.1007/s11883-024-01229-z.

[5] M. Satny, J.A. Hubacek, M. Vrablik, Statins and Inflammation, Curr Atheroscler Rep. 23 (2021) 80. https://doi.org/10.1007/s11883-021-00977-6.

[6] K. Kim, H.N. Ginsberg, S.H. Choi, New, Novel Lipid-Lowering Agents for Reducing Cardiovascular Risk: Beyond Statins, Diabetes Metab J. 46 (2022) 517-532. https://doi.org/10.4093/dmj.2022.0198.

[7] J.J. Li, H.H. Liu, N.Q. Wu, et al., Statin intolerance: an updated, narrative review mainly focusing on muscle adverse effects, Expert Opin Drug Metab Toxicol. 16 (2020) 837-851. https://doi.org/10.1080/17425255.2020.1802426.

[8] B.E. Katamesh, A.A. Mickow, L. Huang, et al., Overcoming patient reluctance to statin intolerance, Kardiol Pol. 82 (2024) 485-491. https://doi.org/10.33963/v.phj.100526.

[9] M. Xiao, T. Zhang, F. Cao, et al., Anti-influenza properties of tiliroside isolated from Hibiscus mutabilis L, J Ethnopharmacol. 303 (2023) 115918. https://doi.org/10.1016/j.jep.2022.115918.

[10] T. Goto, M. Horita, H. Nagai, et al., Tiliroside, a glycosidic flavonoid, inhibits carbohydrate digestion and glucose absorption in the gastrointestinal tract, Mol Nutr Food Res. 56 (2012) 435-445. https://doi.org/10.1002/mnfr.201100458.

[11] Y.-J. Zhou, Q. Ren, Y.-B. Shen, Comprehensive review of Tilia L.: phytochemical profiles, edible value, therapeutic potentials, and ecological significance, Food & Medicine Homology. 2 (2025) 9420035. https://doi.org/10.26599/FMH.2025.9420035.

[12] T. Goto, A. Teraminami, J.Y. Lee, et al., Tiliroside, a glycosidic flavonoid, ameliorates obesity-induced metabolic disorders via activation of adiponectin signaling followed by enhancement of fatty acid oxidation in liver and skeletal muscle in obese-diabetic mice, J Nutr Biochem. 23 (2012) 768-776. https://doi.org/10.1016/j.jnutbio.2011.04.001.

[13] R. Velagapudi, A. El-Bakoush, O.A. Olajide, Activation of Nrf2 Pathway Contributes to Neuroprotection by the Dietary Flavonoid Tiliroside, Mol Neurobiol. 55 (2018) 8103-8123. https://doi.org/10.1007/s12035-018-0975-2.

[14] X. Feng, Y. Qin, S. Ma, et al., Liubao tea extract restrains obesity-related hyperlipidemia via regulation of AMPK/p38/NF-κB pathway and intestinal microbiota, Food Chem. 464 (2025) 141910. https://doi.org/10.1016/j.foodchem.2024.141910.

[15] D.M. Grochowski, M. Locatelli, S. Granica, et al., A Review on the Dietary Flavonoid Tiliroside, Compr Rev Food Sci Food Saf. 17 (2018) 1395-1421. https://doi.org/10.1111/1541-4337.12389.

[16] A. Nagatomo, M. Oguri, N. Nishida, et al., Evaluation of genotoxicity and subchronic toxicity of standardized rose hip extract, Hum Exp Toxicol. 37 (2018) 725-741. https://doi.org/10.1177/0960327117730881.

[17] F. Wang, Z. Zhang, A. Fang, et al., Macrophage Foam Cell-Targeting Immunization Attenuates Atherosclerosis, Front Immunol. 9 (2018) 3127. https://doi.org/10.3389/fimmu.2018.03127.

[18] B. Wang, X. Tang, L. Yao, et al., Disruption of USP9X in macrophages promotes foam cell formation and atherosclerosis, J Clin Invest. 132 (2022) https://doi.org/10.1172/jci154217.

[19] X. Liu, J. Wu, R. Tian, et al., Targeting foam cell formation and macrophage polarization in atherosclerosis: The Therapeutic potential of rhubarb, Biomed Pharmacother. 129 (2020) 110433. https://doi.org/10.1016/j.biopha.2020.110433.

[20] X. Xia, Q. Xu, M. Liu, et al., Deubiquitination of CD36 by UCHL1 promotes foam cell formation, Cell Death Dis. 11 (2020) 636. https://doi.org/10.1038/s41419-020-02888-x.

[21] A.J. Kattoor, S.H. Kanuri, J.L. Mehta, Role of Ox-LDL and LOX-1 in Atherogenesis, Curr Med Chem. 26 (2019) 1693-1700. https://doi.org/10.2174/0929867325666180508100950.

[22] S.J. Chen, Y.H. Kao, L. Jing, et al., Epigallocatechin-3-gallate Reduces Scavenger Receptor A Expression and Foam Cell Formation in Human Macrophages, J Agric Food Chem. 65 (2017) 3141-3150. https://doi.org/10.1021/acs.jafc.6b05832.

[23] P. Libby, The changing landscape of atherosclerosis, Nature. 592 (2021) 524-533. https://doi.org/10.1038/s41586-021-03392-8.

[24] D. Wang, Y. Yang, Y. Lei, et al., Targeting Foam Cell Formation in Atherosclerosis: Therapeutic Potential of Natural Products, Pharmacol Rev. 71 (2019) 596-670. https://doi.org/10.1124/pr.118.017178.

[25] S. Tang, Q. Yu, C. Ding, Investigational spleen tyrosine kinase (SYK) inhibitors for the treatment of autoimmune diseases, Expert Opin Investig Drugs. 31 (2022) 291-303. https://doi.org/10.1080/13543784.2022.2040014.

[26] S.R. Savla, K.S. Prabhavalkar, L.K. Bhatt, Liver X receptor: a potential target in the treatment of atherosclerosis, Expert Opin Ther Targets. 26 (2022) 645-658. https://doi.org/10.1080/14728222.2022.2117610.

[27] A. Javadifar, S. Rastgoo, M. Banach, et al., Foam Cells as Therapeutic Targets in Atherosclerosis with a Focus on the Regulatory Roles of Non-Coding RNAs, Int J Mol Sci. 22 (2021) https://doi.org/10.3390/ijms22052529.

[28] Q. Tang, R. Ratnayake, G. Seabra, et al., Morphological profiling for drug discovery in the era of deep learning, Brief Bioinform. 25 (2024) https://doi.org/10.1093/bib/bbae284.

[29] P.K. Akalin, Introduction to bioinformatics, Mol Nutr Food Res. 50 (2006) 610-619. https://doi.org/10.1002/mnfr.200500273.

[30] S.K. Wooller, G. Benstead-Hume, X. Chen, et al., Bioinformatics in translational drug discovery, Biosci Rep. 37 (2017) https://doi.org/10.1042/bsr20160180.

[31] R.C. Deo, Machine Learning in Medicine, Circulation. 132 (2015) 1920-1930. https://doi.org/10.1161/circulationaha.115.001593.

[32] H. Alonso, A.A. Bliznyuk, J.E. Gready, Combining docking and molecular dynamic simulations in drug design, Med Res Rev. 26 (2006) 531-568. https://doi.org/10.1002/med.20067.

[33] S.A. Hollingsworth, R.O. Dror, Molecular Dynamics Simulation for All, Neuron. 99 (2018) 1129-1143. https://doi.org/10.1016/j.neuron.2018.08.011.

[34] R. Edgar, M. Domrachev, A.E. Lash, Gene Expression Omnibus: NCBI gene expression and hybridization array data repository, Nucleic Acids Res. 30 (2002) 207-210. https://doi.org/10.1093/nar/30.1.207.

[35] A. Subramanian, P. Tamayo, V.K. Mootha, et al., Gene set enrichment analysis: a knowledge-based approach for interpreting genome-wide expression profiles, Proc Natl Acad Sci U S A. 102 (2005) 15545-15550. https://doi.org/10.1073/pnas.0506580102.

[36] P. Langfelder, S. Horvath, WGCNA: an R package for weighted correlation network analysis, BMC Bioinformatics. 9 (2008) 559. https://doi.org/10.1186/1471-2105-9-559.

[37] G.M. Morris, R. Huey, W. Lindstrom, et al., AutoDock4 and AutoDockTools4: Automated docking with selective receptor flexibility, J Comput Chem. 30 (2009) 2785-2791. https://doi.org/10.1002/jcc.21256.

[38] O. Trott, A.J. Olson, AutoDock Vina: improving the speed and accuracy of docking with a new scoring function, efficient optimization, and multithreading, J Comput Chem. 31 (2010) 455-461. https://doi.org/10.1002/jcc.21334.

[39] R. Kumari, R. Kumar, A. Lynn, g_mmpbsa--a GROMACS tool for high-throughput MM-PBSA calculations, J Chem Inf Model. 54 (2014) 1951-1962. https://doi.org/10.1021/ci500020m.

[40]J. Friedman, T. Hastie, R. Tibshirani, Regularization Paths for Generalized Linear Models via Coordinate Descent, J Stat Softw. 33 (2010) 1-22.

[41] D.F. Schwarz, I.R. König, A. Ziegler, On safari to Random Jungle: a fast implementation of Random Forests for high-dimensional data, Bioinformatics. 26 (2010) 1752-1758. https://doi.org/10.1093/bioinformatics/btq257.

[42] X. Robin, N. Turck, A. Hainard, et al., pROC: an open-source package for R and S+ to analyze and compare ROC curves, BMC Bioinformatics. 12 (2011) 77. https://doi.org/10.1186/1471-2105-12-77.

[43] A.M. Newman, C.L. Liu, M.R. Green, et al., Robust enumeration of cell subsets from tissue expression profiles, Nat Methods. 12 (2015) 453-457. https://doi.org/10.1038/nmeth.3337.

[44] K. Yoshihara, M. Shahmoradgoli, E. Martínez, et al., Inferring tumour purity and stromal and immune cell admixture from expression data, Nat Commun. 4 (2013) 2612. https://doi.org/10.1038/ncomms3612.

[45] Y. Hao, S. Hao, E. Andersen-Nissen, et al., Integrated analysis of multimodal single-cell data, Cell. 184 (2021) 3573-3587.e3529. https://doi.org/10.1016/j.cell.2021.04.048.

[46] H. Zhuang, Q. Lv, C. Zhong, et al., Tiliroside Ameliorates Ulcerative Colitis by Restoring the M1/M2 Macrophage Balance via the HIF-1α/glycolysis Pathway, Frontiers in Immunology. Volume 12 - 2021 (2021), https://www.frontiersin.org/journals/immunology/articles/10.3389/fimmu.2021.649463

[47] R. Han, H. Yang, C. Ling, L. Lu, Tiliroside suppresses triple-negative breast cancer as a multifunctional CAXII inhibitor, Cancer Cell International. 22 (2022) 368. https://doi.org/10.1186/s12935-022-02786-6.

[48] F. Cai, K. Zhou, P. Wang, et al., A novel KEAP1 inhibitor, tiliroside, activates NRF2 to protect against acetaminophen-induced oxidative stress and acute liver injury, Hepatol Commun. 9 (2025) https://doi.org/10.1097/hc9.0000000000000658.

[49] M. Xu, W. Zhong, C. Yang, et al., Tiliroside disrupted iron homeostasis and induced ferroptosis via directly targeting calpain-2 in pancreatic cancer cells, Phytomedicine. 127 (2024) 155392. https://doi.org/10.1016/j.phymed.2024.155392.

[50] Y.Y. Qiu, J. Zhang, F.Y. Zeng, Y.Z. Zhu, Roles of the peroxisome proliferator-activated receptors (PPARs) in the pathogenesis of nonalcoholic fatty liver disease (NAFLD), Pharmacol Res. 192 (2023) 106786. https://doi.org/10.1016/j.phrs.2023.106786.

[51] Y. Cao, X. Chen, F. Pan, et al., Xinmaikang-mediated mitophagy attenuates atherosclerosis via the PINK1/Parkin signaling pathway, Phytomedicine. 119 (2023) 154955. https://doi.org/10.1016/j.phymed.2023.154955.

[52] Y. Yang, S. Chen, G. Shi, et al., Polyphenol extract ameliorates diabetes-related atherosclerosis through HIF-1 signaling pathway in APOE(-/)(-) mice: Possible synergism with atorvastatin, Phytomedicine. 140 (2025) 156572. https://doi.org/10.1016/j.phymed.2025.156572.

[53] R.R. He, C.R. Ma, X. He, et al., Circulating metabolites of Borneolum syntheticum (Bingpian) ameliorate atherosclerosis in ApoE(-/-) mice via inhibiting macrophage foam-cell formation, Acta Pharmacol Sin. 46 (2025) 759-776. https://doi.org/10.1038/s41401-024-01406-5.

[54] F. Liu, S. Shan, H. Li, et al., Millet shell polyphenols ameliorate atherosclerosis development by suppressing foam cell formation, J Nutr Biochem. 115 (2023) 109271. https://doi.org/10.1016/j.jnutbio.2023.109271.

[55] Y. Li, W. Song, Y. Tong, et al., Isoliquiritin ameliorates depression by suppressing NLRP3-mediated pyroptosis via miRNA-27a/SYK/NF-κB axis, J Neuroinflammation. 18 (2021) 1. https://doi.org/10.1186/s12974-020-02040-8.

[56] S. Li, Y. Zhang, R. Lu, et al., Peroxiredoxin 1 aggravates acute kidney injury by promoting inflammation through Mincle/Syk/NF-κB signaling, Kidney Int. 104 (2023) 305-323. https://doi.org/10.1016/j.kint.2023.04.013.

[57] H. Zhuang, Q. Lv, C. Zhong, et al., Tiliroside Ameliorates Ulcerative Colitis by Restoring the M1/M2 Macrophage Balance via the HIF-1α/glycolysis Pathway, Front Immunol. 12 (2021) 649463. https://doi.org/10.3389/fimmu.2021.649463.

[58] F. Cai, D. Li, K. Zhou, et al., Tiliroside attenuates acute kidney injury by inhibiting ferroptosis through the disruption of NRF2-KEAP1 interaction, Phytomedicine. 126 (2024) 155407. https://doi.org/10.1016/j.phymed.2024.155407.

[59] X. Yi, C. Xu, J. Yang, et al., Tiliroside Protects against Lipopolysaccharide-Induced Acute Kidney Injury via Intrarenal Renin-Angiotensin System in Mice, Int J Mol Sci. 24 (2023) https://doi.org/10.3390/ijms242115556.

[60] C. Zhong, J. Yang, K. Deng, et al., Tiliroside Attenuates NLRP3 Inflammasome Activation in Macrophages and Protects against Acute Lung Injury in Mice, Molecules. 28 (2023) https://doi.org/10.3390/molecules28227527.

[61] Y. Dong, X. Xia, M. Wang, et al., Tiliroside from Lagopsis supina Ameliorates Myocardial Ischemia Injury in Zebrafish by Activating the kdr-Mediated PI3K-Akt and MAPK Signaling Pathways, Int J Mol Sci. 26 (2025) https://doi.org/10.3390/ijms26052313.

[62] A. Mócsai, J. Ruland, V.L. Tybulewicz, The SYK tyrosine kinase: a crucial player in diverse biological functions, Nat Rev Immunol. 10 (2010) 387-402. https://doi.org/10.1038/nri2765.

[63] Y. Wu, W. Pan, X. Hu, et al., The prospects for targeting FcR as a novel therapeutic strategy in rheumatoid arthritis, Biochem Pharmacol. 183 (2021) 114360. https://doi.org/10.1016/j.bcp.2020.114360.

[64] A. Llop-Guevara, M. Porras, C. Cendón, et al., Simultaneous inhibition of JAK and SYK kinases ameliorates chronic and destructive arthritis in mice, Arthritis Res Ther. 17 (2015) 356. https://doi.org/10.1186/s13075-015-0866-0.

[65] A.K. Mandal, A. Sahoo, K. Dwivedi, et al., Potential therapeutic application of biophenols - plants secondary metabolites in rheumatoid arthritis, Crit Rev Food Sci Nutr. 63 (2023) 8900-8918. https://doi.org/10.1080/10408398.2022.2062700.

[66] Y. Jiang, Y. Cheng, S. Ma, et al., Systemic lupus erythematosus-complicating immune thrombocytopenia: From pathogenesis to treatment, J Autoimmun. 132 (2022) 102887. https://doi.org/10.1016/j.jaut.2022.102887.

[67] D. Niebel, L. de Vos, T. Fetter, et al., Cutaneous Lupus Erythematosus: An Update on Pathogenesis and Future Therapeutic Directions, Am J Clin Dermatol. 24 (2023) 521-540. https://doi.org/10.1007/s40257-023-00774-8.

[68] K. Ma, W. Du, S. Wang, et al., B1-cell-produced anti-phosphatidylserine antibodies contribute to lupus nephritis development via TLR-mediated Syk activation, Cell Mol Immunol. 20 (2023) 881-894. https://doi.org/10.1038/s41423-023-01049-2.

[69] B. Qian, R. Lu, S. Mao, et al., Podocyte SIRPα reduction aggravates lupus nephritis via promoting T cell inflammatory responses, Cell Rep. 43 (2024) 114249. https://doi.org/10.1016/j.celrep.2024.114249.

[70] M. Mooring, G.A. Yeung, P. Luukkonen, et al., Hepatocyte CYR61 polarizes profibrotic macrophages to orchestrate NASH fibrosis, Sci Transl Med. 15 (2023) eade3157. https://doi.org/10.1126/scitranslmed.ade3157.

[71] C. Qu, D. Zheng, S. Li, et al., Tyrosine kinase SYK is a potential therapeutic target for liver fibrosis, Hepatology. 68 (2018) 1125-1139. https://doi.org/10.1002/hep.29881.

[72] M. Yu, H. Ding, S. Gong, et al., Fungal dysbiosis facilitates inflammatory bowel disease by enhancing CD4+ T cell glutaminolysis, Front Cell Infect Microbiol. 13 (2023) 1140757. https://doi.org/10.3389/fcimb.2023.1140757.

[73] W. Gong, J. Yu, T. Zheng, et al., CCL4-mediated targeting of spleen tyrosine kinase (Syk) inhibitor using nanoparticles alleviates inflammatory bowel disease, Clin Transl Med. 11 (2021) e339. https://doi.org/10.1002/ctm2.339.

[74] C. Hu, X. He, H. Zhang, et al., Tanshinone I limits inflammasome activation of macrophage via docking into Syk to alleviate DSS-induced colitis in mice, Mol Immunol. 173 (2024) 88-98. https://doi.org/10.1016/j.molimm.2024.07.007.

[75] D. Wang, V. Hiebl, D. Schachner, et al., Soraphen A enhances macrophage cholesterol efflux via indirect LXR activation and ABCA1 upregulation, Biochem Pharmacol. 177 (2020) 114022. https://doi.org/10.1016/j.bcp.2020.114022.

[76] M.P.T. Le, C.K. Marasinghe, J.Y. Je, Chitosan oligosaccharides: A potential therapeutic agent for inhibiting foam cell formation in atherosclerosis, Int J Biol Macromol. 282 (2024) 137186. https://doi.org/10.1016/j.ijbiomac.2024.137186.

[77] S. Zheng, H. Huang, Y. Li, et al., Yin-xing-tong-mai decoction attenuates atherosclerosis via activating PPARγ-LXRα-ABCA1/ABCG1 pathway, Pharmacol Res. 169 (2021) 105639. https://doi.org/10.1016/j.phrs.2021.105639.

[78] R. Chen, Y. Zhang, N. Patel, et al., CARD9 mediated MAPK/NF-κB signal pathway participates in the pathophysiological process of septic hepatitis: The role of tiliroside, Int Immunopharmacol. 124 (2023) 110275. https://doi.org/10.1016/j.intimp.2023.110275.

[79] F.K. Alkholifi, S. Devi, M.F. Aldawsari, et al., Effects of Tiliroside and Lisuride Co-Treatment on the PI3K/Akt Signal Pathway: Modulating Neuroinflammation and Apoptosis in Parkinson's Disease, Biomedicines. 11 (2023) https://doi.org/10.3390/biomedicines11102735.

[80]K. Li, Y. Xiao, Z. Wang, et al., Tiliroside is a new potential therapeutic drug for osteoporosis in mice, J Cell Physiol. 234 (2019) 16263-16274. https://doi.org/10.1002/jcp.28289.